Cell Reports

Article

A fitness landscape instability governs the morphological diversity of tip-growing cells

Graphical abstract

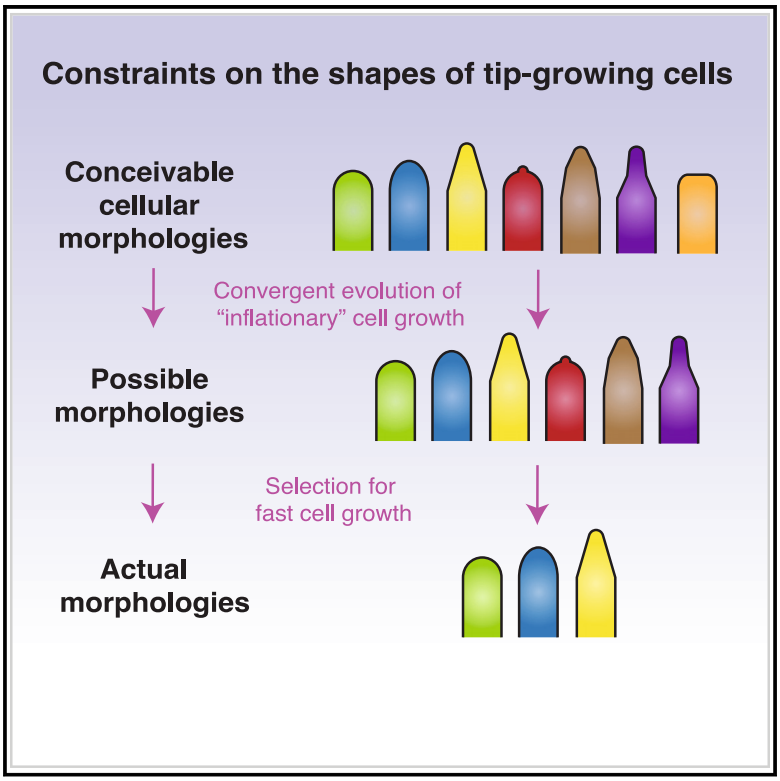

Authors

Maxim E. Ohairwe, Branka D. Živanović, Enrique R. Rojas

Correspondence

rojas@nyu.edu

In brief

Ohairwe et al. demonstrate that an intrinsic mechanical instability in the convergent mechanism of "inflationary" cell growth shared by diverse tip-growing cells leads to a bifurcation (branching) of their fitness landscape. This bifurcation strictly constrains natural tip-growing cell shapes.

Highlights

- Diverse tip-growing cells grow by inflating themselves with turgor pressure
- There is an intrinsic mechanical instability in the mechanism of inflationary growth
- The instability leads to a bifurcation of the fitness landscape of tip growth
- The bifurcation strictly constrains observable cell shapes from across nature

Ohairwe et al., 2024, Cell Reports ■■, 113961
■■, 2024 © 2024
https://doi.org/10.1016/j.celrep.2024.113961

CellPress

Please cite this article in press as: Ohairwe et al., A fitness landscape instability governs the morphological diversity of tip-growing cells, Cell Reports (2024), https://doi.org/10.1016/j.celrep.2024.113961

Cell Reports

CellPress
OPEN ACCESS

Article

A fitness landscape instability governs the morphological diversity of tip-growing cells

Maxim E. Ohairwe,[1] Branka D. Živanović,[2] and Enrique R. Rojas[1,3,*]
[1]Department of Biology, New York University, New York, NY 10003, USA
[2]Institute for Multidisciplinary Research, University of Belgrade, Belgrade, Serbia
[3]Lead contact
*Correspondence: rojas@nyu.edu
https://doi.org/10.1016/j.celrep.2024.113961

SUMMARY

Cellular morphology affects many aspects of cellular and organismal physiology. This makes it challenging to dissect the evolutionary basis for specific morphologies since various cellular functions may exert competing selective pressures on this trait, and the influence of these pressures will depend on the specific mechanisms of morphogenesis. In this light, we combined experiment and theory to investigate the complex basis for morphological diversity among tip-growing cells from across the tree of life. We discovered that an instability in the widespread mechanism of "inflationary" tip growth leads directly to a bifurcation in the common fitness landscape of tip-growing cells, which imposes a strict global constraint on their morphologies. This result rationalizes the morphology of an enormous diversity of important fungal, plant, protistan, and bacterial systems. More broadly, our study elucidates the principle that strong evolutionary constraints on complex traits, like biological form, may emerge from emergent instabilities within developmental systems.

INTRODUCTION

It is often taken for granted that cellular morphology is functional,[1] and yet in relatively few cases has the function or the selective advantage of this trait been explicitly demonstrated.[2,3] The comma shape of *Vibrio cholerae* cells, for one example, aids the "corkscrewing" of this bacterial pathogen into the host epithelium. In another case, the highly variable crescent morphology of fish keratocytes emerges from the cytoskeletal dynamics that drive their motility, leading to a correlation between morphology and motility rate.[4] However, while there are many other examples of correlations between morphology and cell state, type, or function,[5–7] these correlations do not necessarily mean that morphology serves a specific function.

On the contrary, morphology typically affects many critical functions that cells perform. For example, during fungal, plant, and animal development, cellular morphology influences the assembly of the cytoskeleton,[8–12] which governs myriad subcellular processes. Similarly, neuronal morphology affects action-potential propagation,[13] neuronal connectivity,[14] and signal integration.[15] Therefore, in general, morphology is likely to be subject to many competing evolutionary pressures, whose effects will also be constrained by the mechanisms of cellular morphogenesis. Given this complexity, a major challenge in biology is to identify and quantitatively weigh the multiple evolutionary and developmental factors that determine cellular morphology for a given system.

Tip-growing cells (Figure 1) provide an instructive example of the complex morphology-function question. These cells are found in a polyphyletic group of species that encompasses nearly all fungi, many important protistan pathogens, pollen tubes and root hairs in plants, as well as the phylum of bacteria that produces our best antibiotics. On one hand, it is clear that the filamentous morphology of tip-growing cells is intimately tied to their common function, which is to locate and consume nutrients (or deliver the gamete in the case of pollen tubes). On the other hand, the apical morphology of tip-growing cells is variable (Figures 1A and S1A), and it is completely unknown whether specific morphologies contribute to cellular function(s) or if this variation simply reflects non-adaptive variation in the underlying mechanisms of morphogenesis. This question is particularly compelling for tip-growing cells since they arose many times via convergent evolution.

Evolutionary developmental biology was conceived to address similar questions in animal systems, but the classic concepts and tools from this field have rarely been applied to single-cell morphology. A central tenet of evolutionary developmental biology is that in order to understand morphological diversity across species, it is critical to understand the mechanistic variation in their developmental programs. A valuable method that emerged from this field was the "theoretical morphospace,"[16] a comparative strategy commonly used to interpret constraints on organismal morphology.[17,18] In this light, our goal was to dissect the complex basis for the morphology of tip-growing cells by combining a mechanistic investigation of their morphogenesis with a top-down analysis of their morphological variation across taxa.

The morphology of tip-growing cells is defined by the geometry of the polysaccharide cell wall (Figure 1C). Because cell-wall geometry is determined by the apical cell-wall expansion that

Please cite this article in press as: Ohairwe et al., A fitness landscape instability governs the morphological diversity of tip-growing cells, Cell Reports (2024), https://doi.org/10.1016/j.celrep.2024.113961

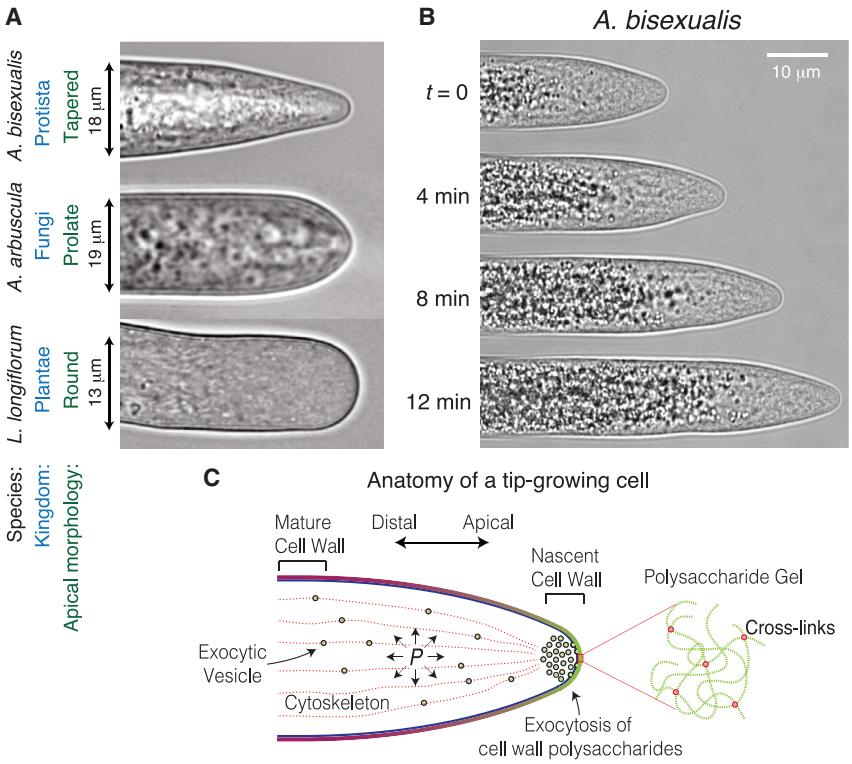

Figure 1. Tip-growing cells are found in diverse taxa

(A) Phase-contrast micrographs of three tip-growing systems.

(B) Time-lapse montage of an *Achlya bisexualis* (*A.b.*) hypha elongating.

(C) The generic features of tip growth. *P* is the turgor pressure.

also leads to cell growth, morphogenesis and growth are the same process for these cells. In most cases, tip growth is self-similar such that apical morphology is approximately constant (Figures 1B and 2A). Therefore, the coordinated steady-state synthesis, metabolism, and physical expansion of the apical cell wall are key processes underlying tip-growth morphogenesis.

Tip-growing cells restrict cell-wall synthesis to the cell apex via localized exocytosis of cell-wall polysaccharides (Figure 1C),[19,20] which is dependent on the actin cytoskeleton in eukaryotic systems.[21–23] The coordination of exocytosis with cell-wall expansion typically relies on a spatial gradient of cell-wall biochemistry whereby the nascent, expanding cell wall is biochemically distinct from the mature, non-expanding wall (Figure 1C).[24–26] For example, during pollen-tube growth, enzymes that prevent cell-wall cross-linking are packaged into the same exocytic vesicles that contain wall polysaccharides,[27] ensuring that the nascent cell wall is mechanically soft.[24] Pollen-tube growth, in turn, depends on the irreversible stretching of the soft apical cell wall by the turgor pressure within the cell (Figure 1C).[28] As for pollen tubes, the growth of fission yeast and the mating projections of budding yeast (examples of transient tip growth) are also akin to controlled "inflation" of the cell by turgor pressure.[26,29]

Theoretical studies have demonstrated that inflationary tip growth can, in principle, explain a range of apical morphologies, from round to highly tapered (Figure 1A).[30–32] However, this mechanism was not interrogated experimentally in non-plant species, which are precisely those that exhibit non-round apical morphologies. Similarly, the cellular basis for morphological variability that was proposed by previous theories was not tested. According to one theory, generation of non-round apical morphologies required a large spatial gradient in cell-wall thickness, which is not observed experimentally.[33] Therefore, it is unknown (1) if diverse tip-growing systems use inflationary growth, (2) whether inflationary growth can generate natural morphologies in a manner consistent with underlying cell biology, and (3) whether tip-growing cells from across nature assume all morphologies realizable by inflationary growth.

By addressing these questions, we identified strong mechanistic and evolutionary constraints on the morphological diversity of tip-growing cells from across nature. Through precise mechanical characterization of cell-wall expansion in three divergent tip-growing systems—a protist, a fungus, and a plant—we first confirmed that each of them drives tip growth via inflation. We then systematically generalized previous theoretical models of inflationary growth[30,31] to account for our data, which allowed us to describe the entire morphospace of tip-growing cells on mechanistic grounds. Surprisingly, we found that morphologies from across nature populated a relatively small region of this morphospace. Further analysis revealed that an emergent cusp bifurcation[34] in the morphospace separated fast-growing natural morphologies from slow-growing hypothetical morphologies. We therefore interpret the morphospace as a fitness landscape and conclude that natural selection for fast growth imposes a strong constraint on the morphology of diverse tip-growing cells. Collectively, our results explain the morphological variation of an enormous diversity of important cellular systems. They also explicitly demonstrate a simple but important evolutionary principle: that emergent instabilities in developmental systems can impose strong constraints on complex traits, like biological form.

RESULTS

Tip-growing cells span a low-dimensional morphological space

To understand the morphological variation of tip growth, it was first useful to objectively quantify apical morphology across taxa. To do so, we recorded time-lapse phase-contrast micrographs (Figures 1B; Video S1) of hundreds of tip-growing cells from a broad diversity of organisms including fungi, protists,

Please cite this article in press as: Ohairwe et al., A fitness landscape instability governs the morphological diversity of tip-growing cells, Cell Reports (2024), https://doi.org/10.1016/j.celrep.2024.113961

CellPress
OPEN ACCESS

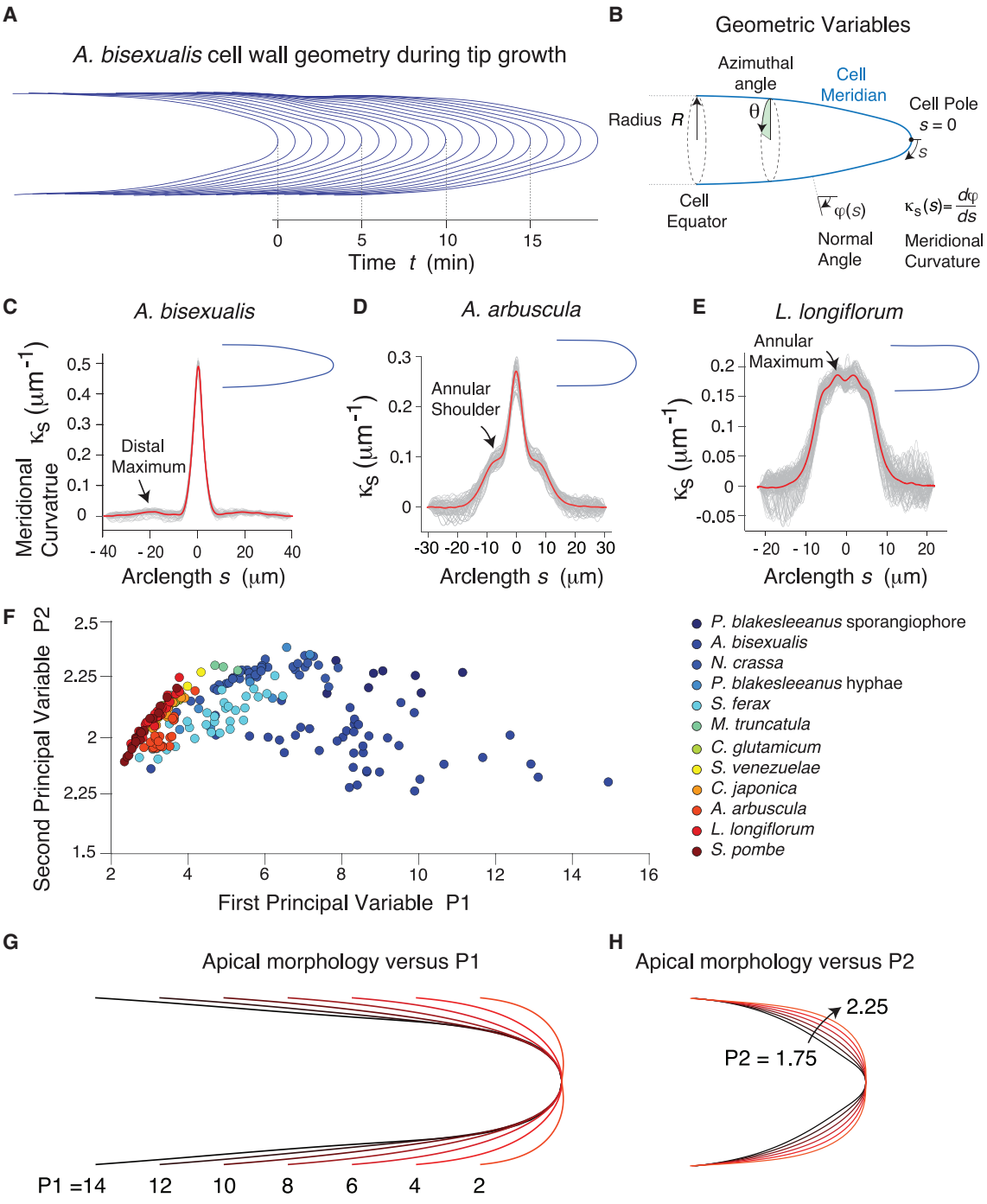

Figure 2. Tip-growing cells exhibit limited morphological variation

(A) Computationally extracted apical geometry versus time from a growing *A.b.* hypha.

(B) Geometric variables of tip growth.

(C–E) Time-averaged meridional curvature versus arclength for *A.b.*, *A. arbuscula* (*A.a.*), and *L. longiflorum* (*L.l.*) (red lines, representative of n = 32, 24, 32, and 32 cells, respectively). Gray traces indicate the meridional curvature profiles from individual time points from which the averages were calculated. (Inset) Reconstructions of the apical morphologies calculated the time-averaged meridional curvature profiles.

(legend continued on next page)

Please cite this article in press as: Ohairwe et al., A fitness landscape instability governs the morphological diversity of tip-growing cells, Cell Reports (2024), https://doi.org/10.1016/j.celrep.2024.113961

plants, and bacteria (Figures 1A and S1A). We then computationally tracked cell-surface geometry from these micrographs (Figure 2A). Position on the cell surface can be described by the coordinates s, the arclength from the cell pole, and θ, the azimuthal angle (Figure 2B). We further quantified apical morphology by calculating the spatial profile of the curvature of a cell "meridian," $\kappa_s(s)$ (Figures 2B–2E).

For all tip-growing cells, the meridional curvature is maximal at or near the cell pole ($s = 0$) and is zero at the cell equator. However, the curvature profiles also revealed species-specific morphological signatures. For example, hyphae of the oomycete *Achlya bisexualis* exhibited a sharp curvature peak near the pole and a slight annular maximum distally, resulting in a tapered apical morphology (Figure 2C). Hyphae of the chytrid fungus *Allomyces arbuscula* exhibited a curvature peak near the pole and annular curvature shoulders, resulting in a prolate morphology (Figure 2D). As was reported previously, the maximum meridional curvature of *Lilium longiflorum* pollen tubes, *Medicago truncatula* root hairs, and *Schizosaccharomyces pombe* cells—each of which has round morphology—occurred in an annulus ≈ 1 μm from the pole (Figures 2E and S2B).[26,28,35]

Despite these fine-scale features, when we applied principal-component analysis to our entire multi-species dataset, the first two principal variables (P1 and P2; Figure 2F) accounted for 99.8% of morphological variation (Figure S1C). Variation in P1 corresponded precisely to scaling of apical morphology along the cell axis (Figures 2G and S1D) and was therefore correlated with the taper of the cell (Figure S1E). Fungal and protistan species featured the highest mean values and the highest variation of P1 (Figure S1F). P2 was inversely related to the taper of the cell independent of axial scaling (Figure 2H). Variation of P1 and P2 alone explained both the annular maximum of pollen tubes and root hairs as well as the annular shoulders of fungal hyphae (Figure S1G), revealing that these species-specific features are manifestations of low-dimensional geometrical variation and demonstrating that P1 and P2 are useful proxies for apical morphology.

Turgor pressure drives tip growth in diverse organisms

Apical morphology is determined by the spatial dependence of cell-wall expansion across the cell apex (Figure 3A). Therefore, we next quantitatively measured this dependence using *A. bisexualis*, *A. arbuscula*, and *L. longiflorum* as model systems since they largely encompass tip-growing morphological and phylogenetic diversity (Figure 1A). To do so, we coated the cell wall with electrically charged fluorescent microspheres and recorded time-lapse phase-contrast and epifluorescence micrographs during tip growth (Figures 3B and 3C; Videos S1 and S2). The cell wall expands along both principal directions (Figure 3A). By computationally analyzing the movement of the microspheres (Figures 3D and S2A–S2E), we precisely calculated the principal expansion-rate profiles, $\dot{\varepsilon}_s(s)$ and $\dot{\varepsilon}_\theta(s)$ (Figures 3E–3G; STAR Methods; Equations 5 and 6).

Although the expansion-rate profiles must vary in order to generate distinct apical morphologies, the profiles from our three model systems all exhibited "azimuthal anisotropy" ($\dot{\varepsilon}_\theta > \dot{\varepsilon}_s$) except for at the pole (where they must be equal due to rotational symmetry) and the equator (where they are both zero). Previous low-resolution measurements of cell-wall expansion in several other tip-growing organisms[26,35–39] were also consistent with azimuthal expansion-rate anisotropy, indicating that this is a widespread feature of tip growth.

To explore the consequences of azimuthal expansion-rate anisotropy on apical morphology, we developed a computational platform to simulate tip growth for a specific pair of principal expansion-rate profiles. We found that azimuthal expansion-rate anisotropy was necessary to generate tapered cells but was not an intrinsic requirement for tip growth (Figures S2F–S2L). It was previously pointed out that azimuthal expansion-rate anisotropy implies that turgor pressure drives cell-wall expansion since the principal tensions in the wall, which balance pressure, also exhibit azimuthal anisotropy ($\lambda_\theta > \lambda_s$) due to the generic filamentous morphology of tip-growing cells.[35,40] To demonstrate this azimuthal tension anisotropy, we explicitly calculated the spatial profiles of the principal tensions from cell-wall geometry (Figures 3H–3J; STAR Methods; Equations 9 and 10).

To explicitly test for inflationary turgor-driven growth, it is not useful to directly compare the principal tension and expansion-rate profiles since the latter are also dependent on the mechanical properties of the cell wall, which are unknown (Figure 3A). To circumvent this issue, we hypothesized that the relative difference between the principal expansion rates will depend only on the relative difference between the principal tensions, regardless of the local mechanical properties. Therefore, we defined the expansion-rate and tension anisotropies quantitatively as $\alpha_{\dot{\varepsilon}} = (\dot{\varepsilon}_\theta - \dot{\varepsilon}_s)/\dot{\varepsilon}_\theta$ and $\alpha_\lambda = (\lambda_\theta - \lambda_s)/\lambda_\theta$. We discovered a precise monotonic scaling between these variables (Figures 3K–3M). Since there is no explanation for this dependence other than that wall expansion is caused by tension, this is strong evidence that inflation underlies tip growth across taxa.

The spatial profile of cell-wall mechanical properties decays over two length scales

Inflationary tip growth means that the spatial expansion-rate profiles (Figures 3E–3G), which lead to specific cell shapes (Figures 2C–2E), result from the spatial profiles of mechanical properties of the cell wall. While it is not possible to measure these properties directly, we inferred them by applying continuum-mechanics-based theory to our experimental data. A

(F) The second principal variable (P2) versus the first principal variable (P1) for each cell from our multi-species principal-component analysis (PCA) dataset (n = 9, 32, 36, 7, 32, 4, 10, 9, 23, 24, 32, and 19 for *P. blakesleeanus* [*P.b.*] sporangiophores, *A.b.*, *N. crassa* [*N.c.*], *P.b.* hyphae, *S. ferax* [*S.f.*], *M. truncatula* [*M.t.*], *C. glutamicum* [*C.g.*], *S. venezuelae* [*S.v.*], *C. japonica* [*C.j.*], *A.a.*, *L.l.*, and *S. pombe* [*S.p.*], respectively).
(G) Apical geometry versus P1. For this calculation, the remaining principal variables were constant and equal to the average experimental value across all cells from all species.
(H) Apical geometry versus P2.

Please cite this article in press as: Ohairwe et al., A fitness landscape instability governs the morphological diversity of tip-growing cells, Cell Reports (2024), https://doi.org/10.1016/j.celrep.2024.113961

CellPress
OPEN ACCESS

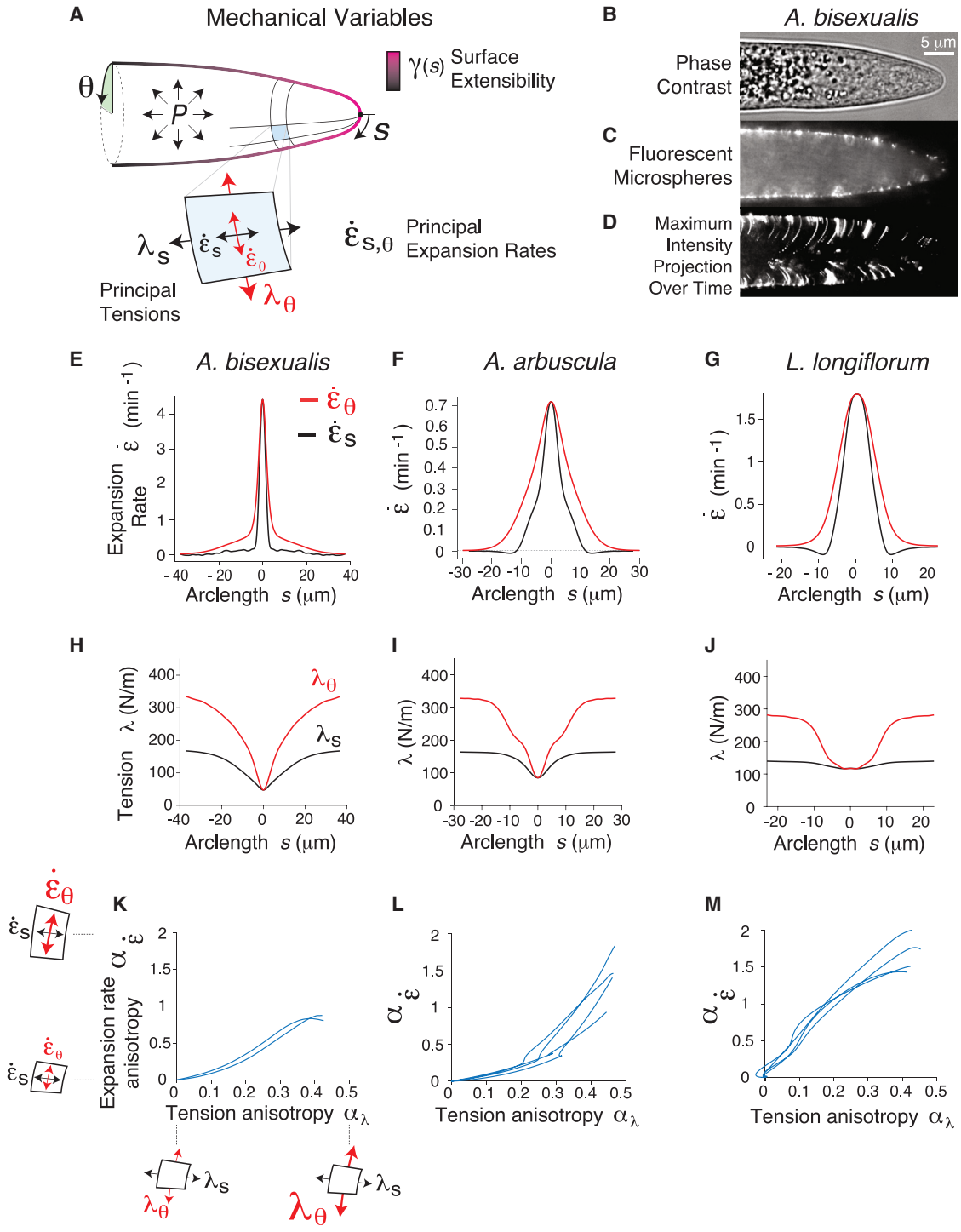

Figure 3. Diverse tip-growing species exhibit azimuthal expansion-rate anisotropy

(A) Mechanical variables of tip growth.

(B) Phase-contrast image of an *A.b.* hypha.

(C) Epifluorescence micrograph of the same hypha in (A) showing fluorescent microspheres attached to the cell wall.

(D) Maximum intensity projection of the epifluorescence time-lapse micrograph from which the image in (C) was selected.

(E–G) Principal cell-wall expansion rates versus arclength for *A.b.*, *A.a.*, and *L.l.* cells (representative of n = 2, 4, and 4 cells, respectively).

(H–J) Principal tensions versus arclength for the cells shown in (E)–(G).

(K–M) Expansion-rate anisotropy versus tension anisotropy across the cell wall. Each trace represents a single cell.

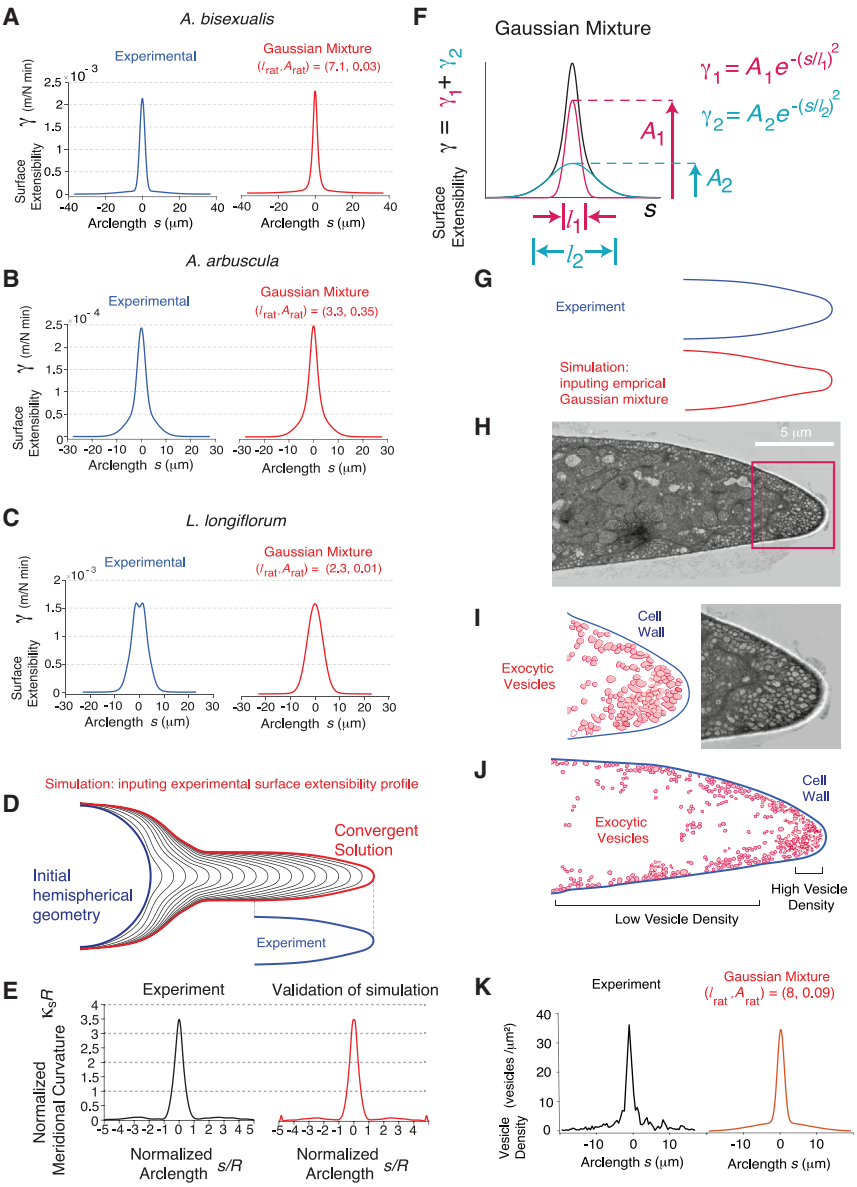

Figure 4. A two-parameter surface extensibility profile accounts for morphological diversity among tip-growing cells

(A–C) (Left) Experimentally determined surface extensibility profiles for *A.b.*, *A.a.*, and *L.l.* (representative of n = 2, 4, and 4 cells, respectively). (Right) Best fit of the experimental surface extensibility profiles by an empirical Gaussian mixture function.

(D) Computational simulation of tip growth based on Equation 1 of the main text, inputting the experimental surface extensibility profile shown in (A, left) and beginning from a hemispherical initial condition.

(E) (Left) The normalized experimental meridional curvature versus normalized arclength. (Right) The normalized meridional curvature of the simulation shown in (D) versus normalized arclength.

(F) The empirical Gaussian mixture function used to fit the surface extensibility profiles.

(G) Comparison of the experimental time-averaged apical morphology of an *A.b.* hypha and the apical morphology of a computational simulation generated with an empirical Gaussian mixture surface extensibility profile shown in (A, right).

(H) Transmission electron micrograph of a thin section of the mid-plane of an *A.b.* hypha.

(I) (Left) Location of exocytic vesicles and cell wall in red box in (H). Zoom of the red boxed region is in (H).

(J) The location of the exocytic vesicles and cell wall in (H).

(K) (Left) The density of vesicles per unit cell-wall length versus arclength (representative of n = 3 cells; see Figure S6A). (Right) Best fit of the experimental vesicle density profile by the empirical Gaussian mixture function.

generic mechanical relationship between principal expansion rates and tensions is one in which they are related linearly[35]:

$$\begin{aligned}\dot{\varepsilon}_s &= \gamma(\lambda_s - \nu\lambda_\theta)\\ \dot{\varepsilon}_\theta &= \gamma(\lambda_\theta - \nu\lambda_s)\end{aligned} \qquad \text{(Equation 1)}$$

The spatially dependent "surface extensibility," $\gamma = \gamma(s)$, determines the cell-wall expansion rate in a given direction if uniaxial tension is applied in that direction (Figure 3A). The "flow coupling," ν, determines the rate at which the wall contracts in one direction due to uniaxial tension in the orthogonal direction. While the cell wall could possess non-linear mechanical properties for large or rapid deformations, this linear implementation of inflationary tip growth will be approximately valid at slow expansion rates characteristic of cell growth. Additionally, we demonstrated that our expansion-rate measurements are inconsistent with structural anisotropy in the cell wall, which could result from oriented synthesis of cell-wall polysaccharides (STAR Methods; Figures S3A and S3B), and that, in any case, such anisotropy would have a negligible effect on the morphospace that inflationary growth yields (Figure S4). Indeed, our linear isotropic implementation of inflationary tip growth (Equation 1) provided accurate, simultaneous fits of the experimental curvature (Figure S5) and expansion-rate profiles (Figures S2C–S2E; STAR Methods) from each cell of each of our model species. Therefore, this formulation of tip growth is a useful tool for exploring its morphospace.

To this end, we derived surface extensibility profiles, $\gamma(s)$, for each model species by substituting their experimental principal expansion-rate and tension profiles into Equation 1 (Figures 4A–4C). These profiles possessed species-specific features that loosely resembled the curvature profiles. In particular, the profiles from *A. bisexualis* and *A. arbuscula* displayed sharp central peaks, while the *L. longiflorum* meridional profile had a slight annular maximum. Both the *A. bisexualis* and *A. arbuscula* azimuthal profiles had clear "shoulders" that

Please cite this article in press as: Ohairwe et al., A fitness landscape instability governs the morphological diversity of tip-growing cells, Cell Reports (2024), https://doi.org/10.1016/j.celrep.2024.113961

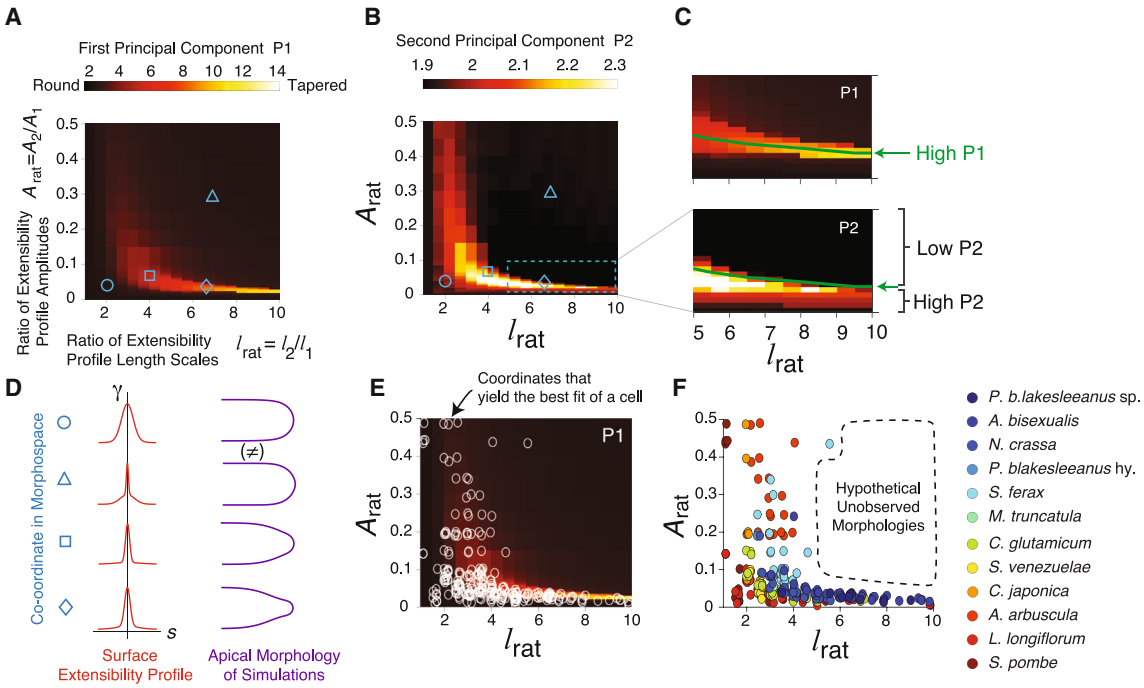

Figure 5. Tip-growing cells exhibit a limited range of possible morphologies

(A) P1 of simulations of inflationary tip growth (Equation 1) inputting an empirical Gaussian mixture surface extensibility profile versus l_{rat} and A_{rat}. A flow coupling of $\nu = 0.5$ was used. P1 is the first principal component of the PCA of our multi-species dataset.

(B) P2 of simulations of inflationary tip growth versus l_{rat} and A_{rat}.

The four blue shapes in (A) and (B) are coordinates of (l_{rat}, A_{rat}) corresponding to surface extensibility profiles and simulated apical morphologies in (D).

(C) Zoom-in of P1 and P2 within the dotted blue box shown in (B). The green line traces the center of the region of high P1.

(D) Surface extensibility profiles and apical morphologies at 4 points in the morphospace shown in (A) and (B).

(E) Coordinates of (l_{rat}, A_{rat}) that, when used to simulate cell growth, yielded the best fit of the geometry for each cell of each species from our multi-species dataset (white circles) overlaid onto the morphospace shown in (A).

(F) Coordinates of (l_{rat}, A_{rat}) that, when used to simulate cell growth, yielded the best fit of the geometry for each cell of each species, color coded by species.

indicated that these profiles decayed to zero over two distinct length scales. Inputting our experimentally derived surface extensibility profiles into our simulation platform generated apical morphologies that were indistinguishable from the experimental morphologies (Figures 4D, 4E, and S5), further supporting the use of the linear implementation of inflationary tip growth (Equation 1).

Given their simple form, we hypothesized that we could accurately fit the surface extensibility profiles with a generic spatial function that was peaked at the cell pole and decayed over two length scales. We first tested a Gaussian mixture (Figure 4F). When the widths (l_1, l_2) and amplitudes (A_1, A_2) of the component Gaussians were used as fitting parameters, this function provided an accurate fit of the profiles (Figures 4A–4C). Furthermore, when we input these fits into our simulation platform, they reproduced accurate apical morphologies: for *A. bisexualis*, the apical geometry of the simulation deviated slightly from the experimental geometry but accurately reproduced the tapered morphology (Figures 4G and S5A), while for *A. arbuscula* and *L. longiflorum*, the difference between the simulated and experimental morphologies was nearly indistinguishable (Figures S5B and S2C). Although a single Gaussian function provided an accurate fit of the *L. longiflorum* apical morphology (Figure S5C), it provided a poor prediction of *A. bisexualis* and *A. arbuscula* morphology, demonstrating the requirement of a two-length-scale surface extensibility profile to generate tapered and prolate apical morphologies. We confirmed that these results did not depend on the specific functional form of the surface extensibility profile by simulating tip growth with non-Gaussian versions (Figure S5).

In light of our analysis, we can summarize a mechanism of morphogenesis of prolate and tapered (i.e., non-round) apical morphologies. When subject to inflation by turgor pressure, a two-length-scale surface extensibility profile, in combination with the intrinsic azimuthal anisotropy of the principal tensions, generates principal expansion-rate profiles that correspond to approximately isotropic expansion near the pole and slow azimuthal expansion in the sub-polar region (Figures 3E and 3F). Such kinetics are necessary and sufficient to generate all non-round apical morphologies, which are characteristic of the vast majority of tip-growing cells.

Exocytic vesicle density predicts cell-wall mechanical properties in *A. bisexualis*

We next sought to explore the ultrastructural and/or biochemical factors that underlie the two length scales associated with the surface extensibility profiles in *A. bisexualis*, as it exhibits highly

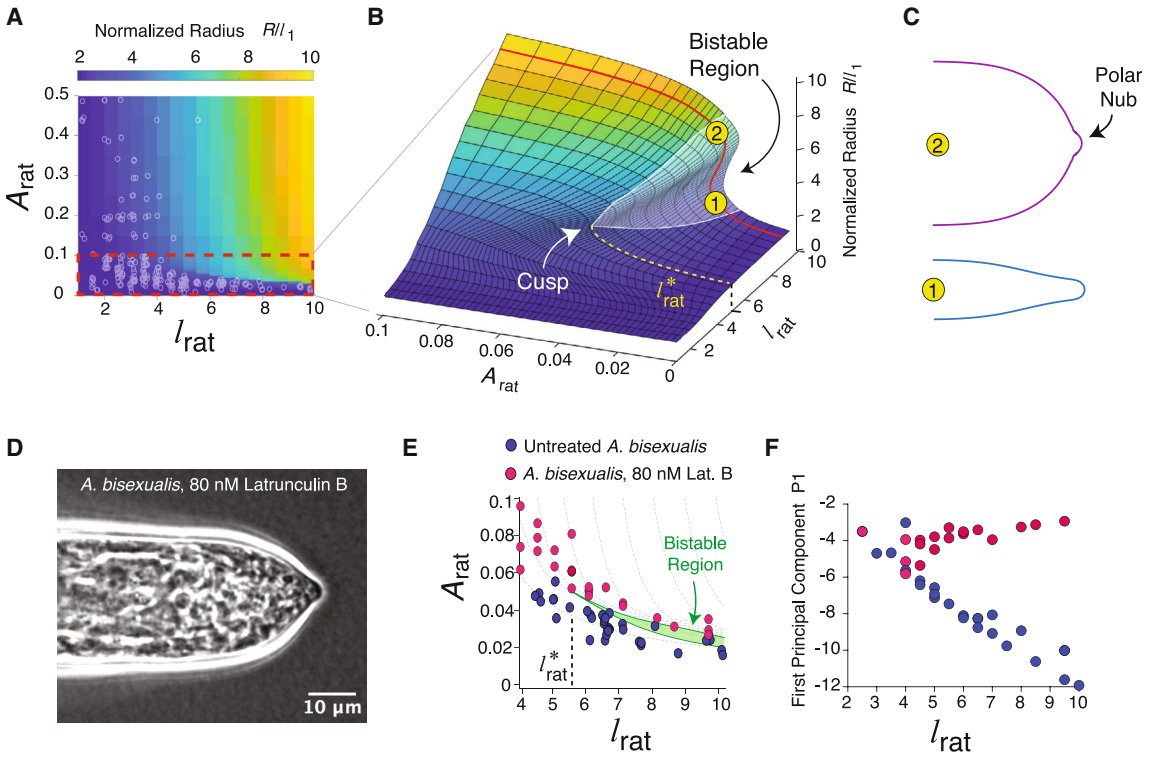

Figure 6. A cusp bifurcation constrains natural tip-growing cell morphologies

(A) Radius of simulated cells, normalized by l_1, as a function of l_{rat} and A_{rat}. The white circles indicate the same coordinates that yielded the best fit of the experimental morphologies shown in Figures 5E and 5F.

(B) Radius of simulated cells, normalized by l_1, versus l_{rat} and A_{rat} within the region enclosed in the red dotted box in (A). The white shaded region indicates the bistable region of the morphospace. l^*_{rat} is the value of l_{rat} above which bistability occurs.

(C) The stable steady-state apical morphologies of simulated cells using a Gaussian mixture surface extensibility profile with $(l_{rat}, A_{rat}) = (9.5, 0.025)$; the only difference between the simulations was the initial condition. The coordinates of the solutions are indicated by the yellow points in (B).

(D) Phase-contrast micrograph of an *A.b.* hypha treated with 80 nM latrunculin B.

(E) Values of (l_{rat}, A_{rat}) that, when used to simulate cell growth, yielded the best fit of the apical geometry for *A.b.* hyphae, comparing untreated hyphae to those treated with 80 nM latrunculin B.

(F) The first principal component of the apical morphology of untreated and latrunculin-B-treated *A.b.* hyphae versus l_{rat}.

tapered hyphae. First, we used transmission electron microscopy to image thin cross-sections of fixed hyphae. In contrast to the predictions of previous theoretical studies, we did not observe a strong gradient in cell-wall thickness (Figure 4H). However, there was a clear spatial dependence of exocytic vesicle distribution within the cytoplasm: near the pole, there was a large pool of vesicles, whereas in the sub-polar region, there was a thin layer of cortical vesicles (Figures 4H–4J). The quantitative spatial dependence of vesicle density showed two clear length scales whose values were consistent with the length scales associated with the surface extensibility profile (Figures 4K and S6A). This supports a model in which exocytosis directly softens the cell wall in this system.

Next, we tested the hypothesis that the two length scales in surface extensibility correspond to two biochemically distinct sections of the cell wall. To do so, we labeled the cell walls of *A. bisexualis* hyphae with the dye direct red 23, which preferentially binds to cellulose, and calcofluor white, which non-specifically binds to β-glucans.[41] Direct red 23 labeling was nearly uniform across the cell apex (Figures S6B and S6C), indicating that variation in cellulose content does not mediate that in wall extensibility. Conversely, calcofluor white labeling was absent in the apical section of the cell wall but increased sharply in the sub-apical section (Figures S6D–S6F). This suggests that synthesis of calcofluor-binding β-glucan(s) may contribute to the determination of the longer of the two length scales associated with the surface extensibility profile. Although cell walls with other compositions (e.g., those of fungi) must necessarily use different mechanisms to set these two length scales, our interrogation of *A. bisexualis* provides a useful basis for comparison.

Diverse tip-growing cells exhibit a limited range of possible apical morphologies

The identification of two length scales in the surface extensibility profiles of our model fungal and protistan systems motivated us to explore the entire theoretical morphospace that a two-length-scale profile could generate. Given such a profile, there are only three scalar parameters that determine apical morphology: ν, $l_{rat} = l_2/l_1$, and $A_{rat} = A_2/A_1$ (Figure 4F; STAR Methods). We simulated tip growth across this parameter space and created a theoretical morphospace for tip growth

Please cite this article in press as: Ohairwe et al., A fitness landscape instability governs the morphological diversity of tip-growing cells, Cell Reports (2024), https://doi.org/10.1016/j.celrep.2024.113961

by calculating the dependence of the principal variables (from our experimental principal-component analysis) on these parameters (Figures 5A–5C). For a given ν, most of the morphospace spanned by l_{rat} and A_{rat} had low values of P1, generating round apical morphologies (Figures 5A–5D). However, there was a narrow region of the morphospace that displayed high values of P1 corresponding to tapered morphologies. Importantly, P1 did not completely determine apical morphology since the region of high P1 separated regions of low P1 that had different values of P2 (Figures 5C and 5D). We found that this morphospace provided an excellent fit of nearly every cell from every species (Figures S7A and S7B).

Variations in the ν shifted the region of tapered morphologies but not the qualitative dependence of P1 on l_{rat} and A_{rat} (Figure S7C). Away from the tapered region, for a given parameter coordinate, ν had little effect on cell morphology (Figure S7D). Furthermore, altering ν had no effect on the fitting power of the model across species (Figure S7B). We conclude that this parameter is not critical for shape determination but rather that l_{rat} and A_{rat} are the key morphogenetic parameters.

Interestingly, we found that the values of l_{rat} and A_{rat} that provided the best fits for the cells in our dataset populated a limited region of the morphospace (Figures 5E and 5F). Furthermore, these (l_{rat}, A_{rat}) coordinates were sharply bounded by the region of tapered morphologies. Importantly, much of the parameter space from which natural shapes were excluded corresponded to round cells with high values of P1, which were qualitatively similar to naturally occuring shapes (Figure 5D); this demonstrates the power of our model to fit fine-scale quantitative features of morphology.

In order to gain insight into this empirical constraint, we analyzed other metrics of cell geometry as a function of l_{rat} and A_{rat}. We discovered that for a given value of l_1 (Figure 4F), cell radius varied as a function of l_{rat} and A_{rat}, with lower values of these variables yielding thinner cells (Figure 6A). Given that low values of l_{rat} and A_{rat} also provided the best fits to experimental apical morphologies (Figures 5E and 5F), this means that cells from across nature are relatively thin compared to the primary length scale of their surface extensibility profile, l_1. While the transition between thin cells to wide ones was gradual as l_{rat} was increased, it was extremely sharp as A_{rat} was increased for $l_{rat} \gtrsim 5$ (Figure 6A).

An instability in the inflationary mechanism of tip growth constrains apical morphology

Sharp changes in the solutions of dynamical systems upon small changes in their parameters often reflect bistability. To explore this possibility, we performed a more fine-scale computational analysis of the region of the morphospace where cell radius changed sharply (Figure 6A, red dotted box). As suspected, the bistable region of a cusp bifurcation[34] emerges in this region (Figure 6B). That is, above a critical value of $l^*_{rat} \approx 5.5$, there is a narrow range of A_{rat} for which two stable apical morphologies exist for a single surface extensibility profile. One of these morphologies is tapered, whereas the other is round but with a nub at the cell pole (Figure 6C). Within the bistable region, the apical morphology on which simulations converged depended on the initial condition (Figures 6C and S7E). Accordingly, for values of $l_{rat} > l^*_{rat}$, the system exhibited hysteresis when A_{rat} was cycled (Figure S7E). Whereas many tip-growing species were confined to the low-radius region of the morphospace by virtue of having low values of l_{rat}, species with tapered apical morphologies (e.g., *A. bisexualis* and *P. blakesleeanus* sporangiophores) had low values of A_{rat} (Figures 6A and S7F) and clustered on the low-radius side of the bistable region.

This bistable region in the morphospace results in what is colloquially known as a "tipping point"[42] with respect to changes in A_{rat}. Intuitively, this tipping point arises due to competition between the two component surface extensibility profiles that comprise the net profile (Figure 4F). The thin and wide profiles, on their own, would each generate round cells with low and high radii, respectively. In the limit that the amplitude of one of these profiles is much greater than the other, the profile with greater amplitude generates a round cell that grows much faster than the one generated by the profile with lower amplitude. On the other hand, for a range of A_{rat}, the two profiles generate cells that grow at similar rates, and therefore competition between these component profiles generate a tapered apical morphology. However, tapered morphologies are nearly unstable because turgor pressure is directionless and will tend to inflate the conical sub-polar region of the cell. Finally, if the component profiles have similar widths (i.e., if l_{rat} is low), then it does not matter which solution grows faster, and the instability disappears at the critical point, or the "cusp" (Figure 6B).

Our analysis made the strong prediction that mild non-specific perturbations might induce tapered cells to cross the tipping point and adopt a round shape with a polar nub (Figure 6C). To test this, we treated *A. bisexualis* hyphae with sub-inhibitory concentrations of latrunculin B, which inhibits actin polymerization. Remarkably, this treatment resulted in stably growing hyphae with apical morphologies qualitatively similar to those predicted by our theory (Figures 6D; Video S3). When fit with our model, latrunculin-B-treated hyphae with l_{rat} values greater than l^*_{rat} now populated the high-radius side of the bistable region (Figure 6E). Therefore, although untreated and treated cells still cluster in the (l_{rat}, A_{rat}) space, their morphologies diverge because they reside on different branches of the manifold of stable apical morphologies (Figure 6F). Finally, latrunculin-B-treated cells were wider than untreated cells, in quantitative agreement with our theory (Figure S8A).

To test whether the shape transitions induced by latrunculin B were perturbation specific, we also measured the effect of sorbitol treatment on *A. bisexualis* tip growth. This osmolyte is thought to induce global softening of the cell wall, which would tend to increase A_{rat} (Figure S8B). Like latrunculin B, sorbitol induced stably growing hyphae to widen and adopt round morphologies with polar nubs (Figures S8C and S8D).

To sum, inflationary tip growth with a two-length-scale surface extensibility profile possesses an intrinsic instability, which predicts a dramatic shape transition that we confirmed experimentally. This is further validation of the (linear isotropic) inflationary mechanism of tip growth since there is no reason to expect this transition otherwise. Furthermore, the form of this instability imposes a strict, empirical constraint on cellular morphology.

The morphospace of tip growth corresponds to a fitness landscape

To understand the reason for this constraint, we next asked how other aspects of cellular physiology depended on morphology.

Please cite this article in press as: Ohairwe et al., A fitness landscape instability governs the morphological diversity of tip-growing cells, Cell Reports (2024), https://doi.org/10.1016/j.celrep.2024.113961

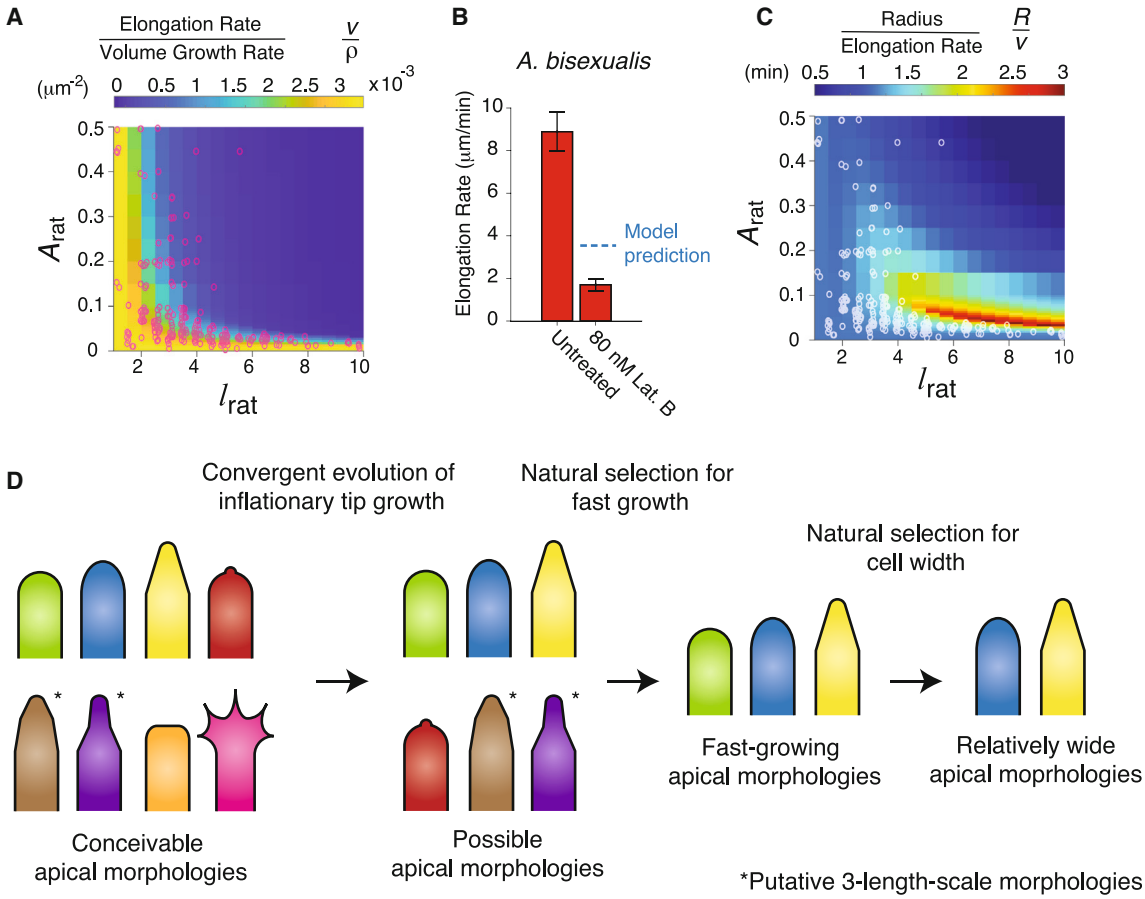

Figure 7. The morphospace of tip-growing cells corresponds to a fitness landscape

(A) The ratio of elongation rate, v, and volume growth rate, ρ, versus l_{rat} and A_{rat} for simulated cells. The red circles indicate the same coordinates that yielded the best fit of the experimental morphologies shown in Figures 5E and 5F.

(B) The population-averaged experimental elongation rate of untreated *A.b.* hyphae and those treated with 80 nM latrunculin B. Error bars indicate ± 1 SD. n = 11 and 9 hyphae for untreated and treated cells, respectively. The dotted line is the prediction of the elongation rate based on the increase in radius (STAR Methods).

(C) The ratio of cell radius and elongation rate versus l_{rat} and A_{rat} for simulated cells.

(D) Illustration of the evolutionary and developmental constraints on the apical morphologies of tip growing cells. Asterisk (*) denotes apical morphologies that are presumed to be possible given a 3-length-scale surface extensibility profile.

Strikingly, we found that the rate of cellular elongation (normalized to the rate of total cell volume enlargement, v/ρ) was inversely related to cell radius. This result has a simple intuitive explanation: that for a given rate of biomass synthesis, a cell can either be thin and elongate rapidly or be wide and elongate slowly. Consistent with this analysis, mild treatments of latrunculin B or sorbitol that caused cells to adopt non-natural wide shapes also caused them to grow more slowly. Although both treatments are likely to have non-specific effects on cellular physiology, they did not reduce the elongation rate much more than our theory predicted (Figures 7B and S8E). The observation that naturally occurring apical morphologies correspond to thin, fast-growing cells—and that hypothetical wide, slow-growing morphologies are mechanistically possible but not observed in nature—strongly suggests that the dependence of elongation rate on the morphogenetic parameters represents a fitness landscape and that variation in the apical morphology of tip-growing systems across the tree of life primarily reflects selection for fast elongation.

In principle, the inverse dependence between growth rate and cell width should hold across populations of cells that display natural variation of these variables. However, we cannot explicitly test this prediction since we cannot control for the metabolic activity of cells, which is a hidden, orthogonal variable that will also affect growth rate. In bacterial systems, it is well understood that global biomass synthesis depends on cell size.[43]

Tapered morphologies balance the benefits of elongation rate and cell radius

Within the limited region of the morphospace that yields fast tip growth, it is possible that the variation in apical morphology reflects selection for specific functions unrelated to growth rate. For example, it has been proposed that tapered morphologies promote invasive growth during pathogenesis,[44] but this intuition has not been tested. We explored an alternate possibility: that tapered morphologies allow hyphae to slightly increase their width beyond that prescribed by the primary length scale of

Please cite this article in press as: Ohairwe et al., A fitness landscape instability governs the morphological diversity of tip-growing cells, Cell Reports (2024), https://doi.org/10.1016/j.celrep.2024.113961

cell-wall expansion. Although cell widening leads intrinsically to reduced elongation rate (Figures 6A and 7A), we reasoned that gradual sub-polar widening could be worth this reduction since fungi and oomycetes transport cytoplasm over long distances via dissipative flow,[45] the energetic cost of which is inversely related to cell radius. To explore this idea, we calculated the cell radius per unit elongation rate, R/v, which quantifies how wide a cell is for a given elongation rate, across our theoretical morphospace. Remarkably, R/v was maximal near the bistable region of the morphospace (Figure 7C), meaning that cells with tapered morphologies not only grew relatively fast but were also relatively wide for a rapidly elongating cell. That is, growing as a tapered cell is a way of simultaneously balancing the benefits v/ρ and R/v.

DISCUSSION

Our analysis revealed three nested determinants of tip-growing morphology (Figure 7D). First, inflationary growth imposes a developmental constraint[46] on the apical morphology of tip-growing cells since morphologies not represented by our theoretical morphospace (Figure 6B) could only be generated by adopting a completely different mechanism of cellular morphogenesis, for example, one where the cytoskeleton generates force. However, the effective pressure that the cytoskeleton can exert is approximately one hundred times smaller than the typical turgor pressure of walled cells.[47] As a result, inflationary growth naturally results from the presence of turgor pressure and the cell wall, which may be viewed as the primary developmental constraints.

Due to the directionless nature of turgor pressure, any surface extensibility profile that decays over a single length scale generates a rounded cell apex. The discovery that tip-growing cells generate profiles that decay over one or two length scales was empirical and inherently constrains apical morphologies. How would adding a third length scale affect morphology? Given our analysis, we propose that this would create the possibility of cell apices with "graduated" taper (Figure 7D). Although these morphologies are possible, we propose that they are essentially just tapered cells and therefore offer no advantage over those generated with a two-length-scale surface extensibility profile. If so, one- and two-length-scale surface extensibility profiles generate the entire space of "useful" morphological variation.

Our most sweeping discovery was that an instability in inflationary tip growth imposes a second, strong constraint on morphology. Tip-growing cells are ubiquitous across nature, serve essential functions in agriculture, are the source of many important antibiotics, and are serious pathogens of humans, crops, and fish. The finding of a widespread constraint on their morphology may have implications in any of these domains.

For example, our analysis demonstrated that highly tapered apical morphologies are nearly unstable (Figure 6), which implicitly suggests that taper serves an important function. One proposed function is that tapered morphologies "knife" through host tissue during the invasive growth of oomycete pathogens.[44] Strictly speaking, this analogy breaks down when comparing the mechanics of knives and cells: while mechanical stress applied by a knife increases with sharpness, mechanical stress applied by a tip-growing cell equals the turgor pressure regardless of taper. We suggest an alternative function of taper: that it yields the widest possible rapidly elongating cells (Figure 7C). The mycelia of many fungi and oomycetes grow as connected networks of hyphae in which cytoplasm moves via gross mass transport over macroscopic distances, a process that is energetically expensive for thin hyphae.[45] Interestingly, oomycetes exhibit large intraspecific variation in hyphal radius and taper (Figure 2F).[32] Based on our analysis, we predict that highly tapered cells act as arterial hyphae that supply less-tapered hyphae with cytoplasm.

The global constraint on apical cell morphology imposed by the cusp bifurcation only makes sense if we interpret the dependence of the elongation rate on the morphospace as a fitness landscape (Figure 7A). In other words, the assertion that fast tip growth is selected for by nature is a major inferential result of our analysis. On one hand, this is a simple conclusion that makes sense in terms of the ecology of these cells: fungal, oomycete, and bacterial hyphae are the vegetative cells that compete within and between species to locate and consume nutrients. On the other hand, this a profound result that provides a window into the ecology—and rationalizes the morphology—of an enormous diversity of interesting and important species. It is well understood that instabilities can dramatically affect the dynamics of ecological systems.[48,49] Similar dynamics in evolutionary systems have been predicted to exist theoretically.[50] Here, we explicitly demonstrate that an intrinsic instability in a widespread developmental mehcanism (inflationary growth) leads to a bifurcation in a fitness landscape, which acts like an "evolutionary fence" that strongly constrains a complex phenotype (cellular morphology).

In the language of life-history theory, selection for fast growth at the expense of morphological variation implies that tip-growing cells have undergone "*r*-selection," meaning that morphology is primarily selected insofar as it is correlated with rapid growth, in order to capitalize on resource abundance.[51] Therefore, just as the "function" of the shape of a dolphin is largely to minimize hydrodynamic drag (an external force), the main function of the morphology of tip-growing cells is to maximize the effect of turgor pressure (an internal force). More broadly, the real question is not whether cell morphology or growth rate is selected for—these are both crucial, complex phenotypes that will be pulled by natural selection in various ways for various reasons. Rather, we sought to explicitly quantify how such complex phenotypes interact in the context of evolution. In the case of tip-growing cells, growth rate won the evolutionary tug of war, which, however, still left room for functional morphological variation, particularly with respect to cell width.

Finally, our analysis provides a case study in how the interaction of physical principles with natural selection sculpts biological form. Since turgor pressure is directionless, inflationary growth tends to generate rounded apices for the same reason that balloons are roughly round. Given inflationary growth, certain morphologies elongate faster than others, and natural selection acts on this widespread developmental constraint. Therefore, tip-growth morphogenesis specifically depends on the direct interplay between a fundamental physical principle (minimization of surface energy) and a fundamental evolutionary principle (fast reproduction outcompetes slow

reproduction). As D'Arcy Thompson predicted, "the manifestations of adaptation become part of a mechanical philosophy" in which "*la Nature agit toujours par les moyens les plus simples*" but also "*chaque chose finit toujours par s'accommoder a son milieu*."[52]

Limitations of the study

In this study, we were inherently limited in the number of systems that we could interrogate with a given assay. For example, to demonstrate inflationary growth, we assayed cell-wall mechanics in three species (Figure 3). However, inflationary growth has been observed many times in walled cells, including fission yeast, algae, and plant tissue.[26,28,29,35,53] In this light, our manuscript reinforces the robust coevolution between inflationary growth and cell walls. We find it likely that there are cellular systems that perform polar growth but do not obey the shape constraints we have described. However, we expect that such systems will be the exceptions that prove the rule: our model predicts that tip-growing cells not employing inflationary growth will be precisely those that violate the constraint imposed by the instability. Similarly, if fast growth were not selected for, our analysis would not apply. Consider neuronal axons as a (somewhat contrived) demonstration of these arguments. Axons use the cytoskeleton to drive polar "tip" growth, and it is unlikely that speed of growth is a strong selective pressure. It is unsurprising then that, qualitatively, they appear to violate the shape constraint we discovered for walled tip-growing cells.

A second limitation is that we explicitly analyzed tip-growing cells executing self-similar unidirectional growth at a constant rate. It will be interesting to apply similar analyses to cells exhibiting oscillatory growth[28] or actively changing their growth direction during chemotropism; such cells are sure to exhibit a wider range of morphologies.

STAR★METHODS

Detailed methods are provided in the online version of this paper and include the following:

SUPPLEMENTAL INFORMATION

Supplemental information can be found online at https://doi.org/10.1016/j.celrep.2024.113961.

ACKNOWLEDGMENTS

We thank the NYU Microscopy Laboratory for assistance with electron microscopy, NIH/NCI P30CA016087 and NIH S10 OD019974. We thank Jacques Dumais for helpful discussions. E.R.R. and M.O.E. were supported by NSF-CAREER grant 2047404. This work was performed in part at the Aspen Center for Physics, NSF grant PHY-221045. B.D.Z. was supported by the Ministry of Education, Science and Technological Development of the Republic of Serbia (451-03-68/2022-14/200053) and the Deutsche Forschungsgemeinschaft (GA 173/13-1).

AUTHOR CONTRIBUTIONS

Conceptualization, E.R.R. and M.E.O; methodology, E.R.R., M.E.O., and B.D.Z.; software, E.R.R.; investigation, E.R.R., M.E.O., and B.D.Z.; writing – original draft, E.R.R. and M.E.O.; writing – review & editing, E.R.R. and M.E.O.; visualization, E.R.R. and M.E.O.; supervision, E.R.R.; funding acquisition, E.R.R.

DECLARATION OF INTERESTS

The authors declare no competing interests.

Received: August 16, 2023
Revised: January 12, 2024
Accepted: February 28, 2024
Published: March 25, 2024

REFERENCES

1. Young, K.D. (2003). Bacterial shape. Mol. Microbiol. *49*, 571–580.
2. Bartlett, T.M., Bratton, B.P., Amit, D., Miguel, A., Sheng, Y., Martin, N.R., Nguyen, J.P., Persat, A., M Desmarais, S., VanNieuwenhze, M.S., et al. (2017). A periplasmic polymer curves vibrio cholerae and promotes pathogenesis. Cell *168*, 172–185.
3. Persat, A., Stone, H.A., and Gitai, Z. (2014). The curved shape of caulobacter crescentus enhances surface colonization in flow. Nat. Commun. *5*, 3824.
4. Keren, K., Pincus, Z., Allen, G.M., Barnhart, E.L., Marriott, G., Mogilner, A., and Theriot, J.A. (2008). Mechanism of shape determination in motile cells. Nature *453*, 475–480.
5. Alizadeh, E., Castle, J., Quirk, A., Taylor, C.D.L., Xu, W., and Prasad, A. (2020). Cellular morphological features are predictive markers of cancer cell state. Comput. Biol. Med. *126*, 104044.
6. Huang, W., Xu, Q., Su, J., Tang, L., Hao, Z.Z., Xu, C., Liu, R., Shen, Y., Sang, X., Xu, N., et al. (2022). Linking transcriptomes with morphological and functional phenotypes in mammalian retinal ganglion cells. Cell Rep. *40*, 111322.
7. Way, G.P., Kost-Alimova, M., Shibue, T., Harrington, W.F., Gill, S., Piccioni, F., Becker, T., Shafqat-Abbasi, H., Hahn, W.C., Carpenter, A.E., et al. (2021). Predicting cell health phenotypes using image-based morphology profiling. Mol. Biol. Cell *32*, 995–1005.
8. Minc, N., Burgess, D., and Chang, F. (2011). Influence of cell geometry on division-plane positioning. Cell *144*, 414–426.
9. Gomez, J.M., Chumakova, L., Bulgakova, N.A., and Brown, N.H. (2016). Microtubule organization is determined by the shape of epithelial cells. Nat. Commun. *7*, 1–13.

10. Sampathkumar, A., Krupinski, P., Wightman, R., Milani, P., Berquand, A., Boudaoud, A., Hamant, O., Jönsson, H., and Meyerowitz, E.M. (2014). Subcellular and supracellular mechanical stress prescribes cytoskeleton behavior in arabidopsis cotyledon pavement cells. Elife *3*, e01967.
11. Kasza, K.E., Farrell, D.L., and Zallen, J.A. (2014). Spatiotemporal control of epithelial remodeling by regulated myosin phosphorylation. Proc. Natl. Acad. Sci. USA *111*, 11732–11737.
12. Beemster, G.T., and Baskin, T.I. (1998). Analysis of cell division and elongation underlying the developmental acceleration of root growth in arabidopsis thaliana. Plant Physiol. *116*, 1515–1526.
13. Waxman, S.G., and Bennett, M.V. (1972). Relative conduction velocities of small myelinated and non-myelinated fibres in the central nervous system. Nat. New Biol. *238*, 217–219.
14. Peichl, L., and Wässle, H. (1983). The structural correlate of the receptive field centre of alpha ganglion cells in the cat retina. J. Physiol. *341*, 309–324.
15. Ronald, AJ. van E., and Arjen van Ooyen. (2010). Impact of dendritic size and dendritic topology on burst firing in pyramidal cells. PLoS Comput. Biol. *6*, e1000781.
16. Raup, D.M. (1966). Geometric analysis of shell coiling: general problems. J. Paleontol., 1178–1190.
17. Stoddard, M.C., Yong, E.H., Akkaynak, D., Sheard, C., Tobias, J.A., and Mahadevan, L. (2017). Avian egg shape: Form, function, and evolution. Science *356*, 1249–1254.
18. Chitwood, D.H., and Mullins, J. (2022). A predicted developmental and evolutionary morphospace for grapevine leaves. Quant. Plant Biol. *3*, e22.
19. Bove, J., Vaillancourt, B., Kroeger, J., Hepler, P.K., Wiseman, P.W., and Geitmann, A. (2008). Magnitude and direction of vesicle dynamics in growing pollen tubes using spatiotemporal image correlation spectroscopy and fluorescence recovery after photobleaching. Plant Physiol. *147*, 1646–1658.
20. Walker, S.K., Chitcholtan, K., Yu, Y., Christenhusz, G.M., and Garrill, A. (2006). Invasive hyphal growth: an f-actin depleted zone is associated with invasive hyphae of the oomycetes *Achlya bisexualis* and *Phytophthora cinnamomi*. Fungal Genet. Biol. *43*, 357–365.
21. Lee, Y.J., Szumlanski, A., Nielsen, E., and Yang, Z. (2008). Rho-gtpase–dependent filamentous actin dynamics coordinate vesicle targeting and exocytosis during tip growth. J. Cell Biol. *181*, 1155–1168.
22. Yu, Y.P., Jackson, S.L., and Garrill, A. (2004). Two distinct distributions of f-actin are present in the hyphal apex of the oomycete achlya bisexualis. Plant Cell Physiol. *45*, 275–280.
23. Fu, Y. (2015). The cytoskeleton in the pollen tube. Curr. Opin. Plant Biol. *28*, 111–119.
24. Parre, E., and Geitmann, A. (2005). Pectin and the role of the physical properties of the cell wall in pollen tube growth of solanum chacoense. Planta *220*, 582–592.
25. Gooday, G.W. (1971). An autoradiographic study of hyphal growth of some fungi. Microbiology *67*, 125–133.
26. Abenza, J.F., Couturier, E., James, D., Dickmann, J., Chessel, A., Dumais, J., and Salas, R.E.C. (2015). Wall mechanics and exocytosis define the shape of growth domains in fission yeast. Nat. Commun. *6*, 1–13.
27. Bosch, M., and Hepler, P.K. (2005). Pectin methylesterases and pectin dynamics in pollen tubes. Plant Cell *17*, 3219–3226.
28. Rojas, E.R., Scott, H., and Dumais, J. (2011). Chemically mediated mechanical expansion of the pollen tube cell wall. Biophys. J. *101*, 1844–1853.
29. Banavar, S.P., Gomez, C., Trogdon, M., Petzold, L.R., Yi, T.-M., and Campàs, O. (2018). Mechanical feedback coordinates cell wall expansion and assembly in yeast mating morphogenesis. PLoS Comput. Biol. *14*, e1005940.
30. Dumais, J., Shaw, S.L., Steele, C.R., Long, S.R., and Ray, P.M. (2006). An anisotropic-viscoplastic model of plant cell morphogenesis by tip growth. Int. J. Dev. Biol. *50*, 209–222.
31. Campàs, O., and Mahadevan, L. (2009). Shape and dynamics of tip-growing cells. Curr. Biol. *19*, 2102–2107.
32. Campàs, O., Rojas, E., Dumais, J., and Mahadevan, L. (2012). Strategies for cell shape control in tip-growing cells. Am. J. Bot. *99*, 1577–1582.
33. Shapiro, A., and Mullins, J.T. (2002). Hyphal tip growth in achlya bisexualis. i. distribution of 1, 3-β-glucans in elongating and non-elongating regions of the wall. Mycologia *94*, 267–272.
34. Kuznetsov, Y.A. (1998). Elements of Applied Bifurcation Theory (Springer).
35. Dumais, J., Long, S.R., and Shaw, S.L. (2004). The mechanics of surface expansion anisotropy in *Medicago truncatula* root hairs. Plant Physiol. *136*, 3266–3275.
36. Mine, I., and Okuda, K. (2003). Extensibility of isolated cell walls in the giant tip-growing cells of the xanthophycean alga vaucheria terrestris. Planta *217*, 425–435.
37. Hejnowicz, Z., Heinemann, B., and Sievers, A. (1977). Tip growth: patterns of growth rate and stress in the chara rhizoid. Z. Pflanzenphysiol. *81*, 409–424.
38. Castle, E.S. (1958). The topography of tip growth in a plant cell. J. Gen. Physiol. *41*, 913–926.
39. Chen, J.C.W. (1973). The kinetics of tip growth in the nitella rhizoid. Plant Cell Physiol. *14*, 631–640.
40. Love, A. (1920). A Treatise on the Mathematical Theory of Elasticity (University Press).
41. Anderson, C.T., Carroll, A., Akhmetova, L., and Somerville, C. (2010). Real-time imaging of cellulose reorientation during cell wall expansion in arabidopsis roots. Plant Physiol. *152*, 787–796.
42. Gladwell, M. (2006). The Tipping Point: How Little Things Can Make a Big Difference (Little).
43. Oldewurtel, E.R., Kitahara, Y., and van Teeffelen, S. (2021). Robust surface-to-mass coupling and turgor-dependent cell width determine bacterial dry-mass density. Proc. Natl. Acad. Sci. USA *118*, e2021416118.
44. Bronkhorst, J., Kots, K., de Jong, D., Kasteel, M., van Boxmeer, T., Joemmanbaks, T., Govers, F., van der Gucht, J., Ketelaar, T., and Sprakel, J. (2022). An actin mechanostat ensures hyphal tip sharpness in phytophthora infestans to achieve host penetration. Sci. Adv. *8*, eabo0875.
45. Roper, M., Simonin, A., Hickey, P.C., Leeder, A., and Glass, N.L. (2013). Nuclear dynamics in a fungal chimera. Proc. Natl. Acad. Sci. USA *110*, 12875–12880.
46. Smith, J.M., Burian, R., Kauffman, S., Alberch, P., Campbell, J., Goodwin, B., Lande, R., Raup, D., and Wolpert, L. (1985). Developmental constraints and evolution: a perspective from the mountain lake conference on development and evolution. Q. Rev. Biol. *60*, 265–287.
47. Parekh, S.H., Chaudhuri, O., Theriot, J.A., and Fletcher, D.A. (2005). Loading history determines the velocity of actin-network growth. Nat. Cell Biol. *7*, 1219–1223.
48. Dai, L., Vorselen, D., Korolev, K.S., and Gore, J. (2012). Generic indicators for loss of resilience before a tipping point leading to population collapse. Science *336*, 1175–1177.
49. Deris, J.B., Kim, M., Zhang, Z., Okano, H., Hermsen, R., Groisman, A., and Hwa, T. (2013). The innate growth bistability and fitness landscapes of antibiotic-resistant bacteria. Science *342*, 1237435.
50. Park, S.-C., and Krug, J. (2011). Bistability in two-locus models with selection, mutation, and recombination. J. Math. Biol. *62*, 763–788.
51. Eric, R. (1970). Pianka. On r- and k-selection. Am. Nat. *104*, 592–597.
52. Thompson d'Arcy, W. (2010). On Growth and Form (Cambridge university press).
53. Green, P.B. (1968). Growth physics in *Nitella*: a method for continuous in vivo analysis of extensibility based on a micro-manometer technique for turgor pressure. Plant Physiol. *43*, 1169–1184.
54. Holdaway-Clarke, T.L., Feijó, J.A., Hackett, G.R., Kunkel, J.G., and Hepler, P.K. (1997). Pollen tube growth and the intracellular cytosolic calcium gradient oscillate in phase while extracellular calcium influx is delayed. Plant Cell *9*, 1999–2010.

55. Živanović, Branka D., Luković, Jelena Danilović, Korać, A., Stanić, M., Spasić, Sladjana Z., and Paul, G. (2022). Signal transduction in phycomyces sporangiophores: columella as a novel sensory organelle mediating auxin-modulated growth rate and membrane potential. Protoplasma, 1–19.

56. Dumais, J., Long, S.R., and Shaw, S.L. (2004). The mechanics of surface expansion anisotropy in medicago truncatula root hairs. Plant Physiol. *136*, 3266–3275.

57. Bernal, R., Rojas, E., and Dumais, J. (2007). The mechanics of tip growth morphogenesis: what we have learned from rubber balloons. J. Mech. Mater. Struct. *2*, 1157–1168.

Please cite this article in press as: Ohairwe et al., A fitness landscape instability governs the morphological diversity of tip-growing cells, Cell Reports (2024), https://doi.org/10.1016/j.celrep.2024.113961

STAR★METHODS

KEY RESOURCES TABLE

REAGENT or RESOURCE	SOURCE	IDENTIFIER
Chemicals, Peptides, and Recombinant Proteins		
Latrunculin B	Abcam	ab144291
Latex beads, amine-modified polystrene	Sigma-Aldrich	L9904
Calcofluor White	Sigma-Aldrich	18909
Direct Red23	Sigma-Aldrich	212490
Experimental Models: Organisms/Strains		
Achlya bisexualis	Carolina Biological	155900
Allomyces arbuscula	Carolina Biological	155911
Corynebacterium glutamicum	Theriot Strain Collection	ATCC 13032
Neurospora crassa	Anne Pringle	ATCC 10815
Phycomyces blakeleeanus	Branka Zivanovic	N/A
Saprolegnia ferax	Carolina Biological	156270
Streptomyces venezuelae	Theriot Strain Collection	ATCC 10712
Software and Algorithms		
Custom MATLAB scripts	This Paper	https://doi.org/10.5281/zenodo.10627414

RESOURCE AVAILABILITY

Lead contact

Further information and requests should be directed to the lead contact, Enrique Rojas (rojas@nyu.edu).

Materials availability

All biological materials used in this study are available from the lead contact upon request or from commercial sources.

Data and code availability

- Data reported in this paper is available upon request.
- Custom MATLAB scripts have been deposited in Github and are also available upon request. The published version of record can be found here: https://doi.org/10.5281/zenodo.10627414
- Any additional information required to reanalyze the data reported in this paper is available from the lead contact upon request.

EXPERIMENTAL MODEL AND STUDY PARTICIPANT DETAILS

Growth conditions

All fungal and oomycete cultures were cultured on yeast-malt growth medium (0.3% yeast extract (m/v), 0.3% malt extract, 0.5% peptone, 1% dextrose, and 1% agarose). Phycomyces sporangiophores were grown on potato dextrose agar. Pollen tubes were grown in 15 mM MES, 1.6 mM H_3BO_3, 0.1 mM KCl, 7.5% sucrose (m/v), adjusted to pH 5.3 with 0.1 mM KOH.[54] *S. venezuelae* was cultured in ISP media. *C. glutamicum* was cultured in BHI media.

METHOD DETAILS

Imaging and image analysis

For imaging of *L. longiflorum* and *C. japonica* pollen tubes, 1 h prior to imaging freeze-dried pollen grains grains were germinated in a growth medium. A thin layer (< 1 mm) of solid growth medium (1% low melting point agarose) was deposited onto the bottom of a custom-made chamber, consisting of a dental polymer gasket adhered to a cover glass. While the agarose was still in a molten state, pollen grains were partially embedded in the solid medium by rinsing it with the liquid suspension of grains. The slide chambers were then filled with liquid medium. Cells that emerged from grains affixed to the agarose in this way were likely to grow along the gel-liquid interface.

For imaging fungal and oomycete hyphae (except for *A. arbuscula*) dental-polymer slide chambers were prepared, as above, with 1% low melting point agarose yeast-malt growth medium. After the agarose solidified, the chamber was inoculated with a small block

of agarose from the growing front of the mycelium in the propagation culture. The top of the slide chamber was then sealed with a coverslip. After incubation for 48–72 h at room temperature, the top of the chamber was opened, and filed with liquid medium for imaging.

For imaging *A. arbuscula*, cultures were propagated in cover-glass bottomed Petri dishes (MakTek). The bottom of the dishes were covered in a layer of ≈ 2 mm of solid growth medium (1% agarose) and one edge of this substrate was inoculated. The hyphae grew in the thin layer of liquid between the cover glass and the agarose at the bottom of the dish. Cells were imaged 5–6 days after inoculation.

For imaging of *S. venezuelae*, 5 μL of exponential phase culture was spotted onto a 1% agarose pad that was molded in a FastWell reagent barrier (Grace Biolabs).

For imaging of *C. glutamicum*, exponential phase cells were loaded into a bacterial microfluidic plate (CellASIC) and perfused with BHI media during imaging using the ONIX microfluidic system.

Time lapse images of pollen tubes, fungal and protistan hyphae, and bacterial cells were taken using an Eclipse TI2 inverted microscope (Nikon) and a Prime BSI sCMOS digital camera (Photometrics).

For imaging of *P. blakesleeanus*, a glass vial filled with solid media was inoculated with a heat-shocked spore suspension, and placed on custom stage equipped with 3-D mechanical adjustment and illuminated with an LED light (Tungsram) from above in a temperature-controlled room (22 ° C). Time-lapse images were taken using a digital CMOS camera (MicroQ) attached to the ocular tube of a horizontal stereo microscope (Leitz).[55]

All cell tracking was performed using custom MATLAB scripts. All software used in this study is available upon request.

Cell wall geometry for *S. pombe* and *M. truncatula* root hairs were obtained from previously published datasets.[26,56]

Single-cell geometry and principal components analysis

To extract single-cell apical cell-wall geometry, we calculated the meridional curvature profile $\kappa_s = d\varphi(s)/ds$ of the cell outline (i.e., cross-sectional meridian) extracted from each time point of a time-lapse image sequence (Figures 2A, 2C, and 2D). We then reconstructed the time-averaged apical geometry for each cell by integrating the time-averaged meridional curvature profile:

$$\varphi(s) = \int_0^s \kappa(s)ds \quad \text{(Equation 2)}$$

$$x(s) = \int_0^s \sin(\varphi)ds \quad \text{(Equation 3)}$$

$$y(s) = \int_0^s \cos(\varphi)ds. \quad \text{(Equation 4)}$$

So as to only perform PCA on the apical region and not the distal region, we truncated the outlines using $\varphi = [-0.95\pi/2, 0.95\pi/2]$ as bounds, and then interpolated the outlines with 75 equally spaced fiducial points. We found that $\varphi = 0.95\pi/2$ was the largest cutoff that did not include large portions of the cylindrical region of the cell. The axis of the apex was found by averaging opposing fiducial points on opposite sides of the cell meridian, and the outlines were rotated and translated such that their axes were aligned and that the cell pole was located at the origin. Principal components analysis was then applied to the interpolated (x,y) outlines at these points using the MATLAB command *pca*.

Microsphere imaging and measurement of meridional speed

The meridional speed and expansion rate measurements for *Lilium longiflorum* pollen tubes (Figures 2E, 3G, 3J, and S2E) was published previously.[28] For microsphere experiments related to *A. bisexualis* and *A. arbuscula*, 0.1 μm aminated fluorescent microspheres (Sigma-Aldrich) were included in all media (10^{-4} dilution from stock), including solid media. For *A. bisexualis*, just after the slide chamber was filled with microsphere-containing media prior to imaging, the microspheres had a high affinity for the cell walls and bound to them. As the charges on the microspheres were neutralized, they lost their affinity for the cell wall, making it necessary to re-immerse them in freshly mixed microsphere growth medium every 10–15 min during imaging.

For *A. arbuscula*, a section of the solid media several millimeters in front of the leading edge of the mycelium was excised with a scalpel, forming a well to which microsphere-containing liquid media was added. Over the course of minutes, the microspheres diffused through the liquid layer between the cover glass as the solid media and reached the mycelium, whereupon they adhered to the hyphal cell walls.

For L. *longiflorum* pollen tubes, to adhere the microspheres to cells, a syringe pump was used to load a glass microcapillary (inner diameter ≈ 50 μm) with microsphere-containing media. The microcapillary was mounted on a micromanipulator and was used to address elongating pollen tubes. Pressure was applied manually to the syringe pump to stream microspheres past the growing pollen tubes during growth. After 5–10 s of streaming the suspension past the tip, the exterior of the cell was effectively coated in

microspheres. The microsphere medium was continually streamed past the cells during imaging such that their cell walls were constantly covered as they expanded.

Fluorescent microsphere tracking was performed using custom MATLAB scripts.[28] From the tracks of the microspheres (Figure S2A) and the cell surface geometry, we calculated the meridional speed of the microspheres (Figures S2B–S2D), which is the speed at which the microspheres move along the cell meridian in the frame of reference of the cell pole. To calculate the principal expansion-rate profiles from the experimental measurements of meridional speed, the spatial dependence of the meridional speed was fit with the empirical function $v(\varphi) = v_0 \sin\varphi(1 + c_1\varphi + c_2\varphi^2 + \cdots)$[35]. F-tests were used to determine the maximum number of free parameters, c_i, that could be retained in this function without fitting noise in the data. The principal expansion rates were calculated from the time-averaged cell geometry profile and this fit of the meridional speed profile using the equations:

$$\dot{\varepsilon}_s = \kappa_s \frac{dv_s}{d\varphi} \quad \text{(Equation 5)}$$

$$\dot{\varepsilon}_\theta = \frac{\cos\varphi}{r} v_s \quad \text{(Equation 6)}$$

where $r(s)$ is the local radius, or the radial distance of a point on the cell surface from the cell axis (Figure 2A).

Because the meridional speed and the cell wall geometry specifically determine the principal expansion rates, to fit these spatially dependent variables together is to also fit the principal expansion rates. The free fit of the meridional speed corresponds to the fit of the fully anisotropic mechanical model (Equation 16, below) shown in Figures S2C–S2E. To fit the experimental meridional speed and cell-wall geometry given isotropical mechanical properties (Figures 2C–2E), we followed a method that we previously developed.[57] Note that in previous analyses, isotropical mechanical properties have been distinguished from transverse (in-plane) mechanical properties where the cell walls is stratified in the normal dimension. However, since we used a two-dimensional formulation of cell surface mechanics, there is no difference between these cases.

The principal tensions were calculated from the experimental profiles of the meridional and azimuthal curvatures, using Equations 7, 8, 9, and 10 below. An arbitrary pressure of 1 atm was assumed. This choice does not affect the spatial distributions of the tensions.

Simulations of cell growth and parameter space search

Simulations of tip growth with arbitrary expansion rates or extensibility profile were performed with a custom MATLAB routine. An initial hemispherical geometry was defined with N (an odd number typically between 101 and 301) discrete (x, y) co-ordinates. The arclength, s, was calculated on the geometry, with the polar point defined as $s = 0$ (Figure 2A). The surface extensibility (or expansion-rate) profile(s) to be simulated was then prescribed on these points. The radius of the hemisphere was arbitrary but was generally chosen to be somewhat larger than the largest length scale associated with the extensibility profile.

When the surface extensibility profile was prescribed, at each step of the simulation, first the principal curvatures in the cell wall were calculated[30]:

$$\kappa_s(s) = \frac{\partial\varphi(s)}{\partial s} \quad \text{(Equation 7)}$$

$$\kappa_\theta(s) = \frac{\sin(\varphi(s))}{r(s)} \quad \text{(Equation 8)}$$

where $r(s)$ is the radial distance from the cell axis to the fiducial point. From the principal curvatures, the principal tensionss were calculated using using force-balance equations[35]:

$$\lambda_s(s) = \frac{P}{2\kappa_\theta} \quad \text{(Equation 9)}$$

$$\lambda_\theta(s) = \frac{P}{2\kappa_\theta}\left(2 - \frac{\kappa_s}{\kappa_\theta}\right) \quad \text{(Equation 10)}$$

In general, the turgor pressure was arbitrarily defined since it only affects the global magnitude of the expansion rates, and therefore the rate of tip growth, rather than the cellular morphology. Unless principal expansion rate profiles were prescribed, they were calculated rom the principal tensions using Equation 1 of the main text:

$$\dot{\varepsilon}_s(s) = \gamma(\lambda_s - \nu\lambda_\theta) \quad \text{(Equation 11)}$$

$$\dot{\varepsilon}_\theta(s) = \gamma(\lambda_\theta - \nu\lambda_s) \quad \text{(Equation 12)}$$

To then calculate the velocity of each fiducial point we inverted the kinematic equations[30]:

$$\dot{\varepsilon}_s = v_n\kappa_s + \frac{\partial v_t}{\partial s} \quad \text{(Equation 13)}$$

$$\dot{\varepsilon}_\theta = v_n\kappa_\theta + \frac{v_t\cos(\varphi)}{r} \quad \text{(Equation 14)}$$

where v_n and v_t are the velocity components of the discrete points in the directions normal and tangential to the cell outline. Finally, the displacement of each point $v_n dt$, $v_t dt$ was calculated (where dt was the time between steps), converted to cartesian co-ordinates, and added to the cell geometry to find the updated cell geometry. This updated geometry was smoothed with a smoothing spline (the MATLAB *csaps* command, with smoothing factor 0.9999), which was critical to prevent small errors from causing runaway instabilities. This routine was iterated until cell geometry converged. At each step, the time step was updated to ensure that the displacement at the pole converged to a fixed, small value.

To validate the simulation routine, we input the experimental surface extensibility profiles, which were calculated to perfectly fit the experimental apical morphology.[57] In our simulations, this surface extensibility profile yielded a meridional curvature profile that was indistinguishable from the experimental profile (Figure S5).

For the parameter space searches described in Figure 5 and Figure S7, l_{rat} was varied on the domain $(1, 10)$ at 0.25 increments and A_{rat} was varied on the domain $(0, 0.1)$ at 0.005 increments and the domain $(0.1, 0.5)$ at 0.05 increments. For each value of A_{rat}, the search was initiated at $l_{rat} = 1$ and A_{rat} was increased incrementally to 0.5, using the solution of cell shape from the previous parameter co-ordinate as the initial condition for each simulation.

To resolve the fold bifurcation shown in Figure 6B, we focused on the domain $l_{rat} \in (1, 10)$ (increments of 0.25) and $A_{rat} \in (0, 0.1)$ (increments of 0.0025). We searched the space as before, but both increased and decreased A_{rat} for a given l_{rat}. To resolve the fold bifurcation we found (l_{rat}, A_{rat}) co-ordinates where there were two stable solutions. For each one of these co-ordinates, from the two stable apical geometries, (x_i^1, y_i^1) and (x_i^2, y_i^2), we found ten intermediate geometries $(x_i^1, y_i^1) + n((x_i^2, y_i^2) - (x_i^2, y_i^2))/9$, where $n = 0, 1, \ldots, 9$. We then initiated a simulation with each of these geometries and determined to which stable solution the simulation converged (Figure S7F). An unstable solution was computed to be the mean of neighboring geometries that converged to different stable fixed geometries (dotted line, Figure S7F). From these unstable geometries, the radius could be calculated to calculate the whole manifold of solutions shown in Figure 6B.

To calculate the best fit of the model for each experimental cell geometry, we first found the time-averaged cell outline, which was found by integrating the time-averaged meridional curvature profile using Equations 2, 3, and 4. We discretized the time-averaged experimental cell outline into the same number of points that was used to simulate tip growth in the computational parameter space search. We then calculated the normalized average error,

$$E = \frac{\sum_{i=1}^{N} de_i}{Nds} \quad \text{(Equation 15)}$$

which is the average error of each discretized point relative to the interpoint arclength. We found values of l_{rat} and A_{rat} that minimized this error.

The normalized elongation rate (Figure 7A) was calculated as follows. At steady-state, the total rate at which the cell increases in volume is $\rho = \pi R^2 v$, where R is the cell radius and v is the elongation rate of the cell. Therefore, a normalized form of the elongation rate is $\tilde{v} = \frac{v}{\rho} = \frac{1}{\pi R^2}$. This quantity has dimensions of inverse area: it is the rate at which the cell elongates per unit volume added to the cell. We arbitrarily dimensionalized the morphospace in Figure 7A using the radius of a pollen tube. This specific dimensionalization does not affect the landscape of v.

The dependence of the ratio of cell radius and elongation rate was calculated by first calculating the absolute (un-normalized) radius and elongation rate of the simulations. We then dimensionalized these variables by arbitrarily assuming that cells that are generated by a single-length-scale surface extensibility profile grow with the radius and elongation rate of a pollen tube. This specific dimensionalization does not affect the landscape of R/v.

Theoretical analysis of anisotropical version of the linear extensibility model

Equation 1 of the main text is a generic linear formulation of inflationary tip growth if the wall is isotropic within the plane of the cell wall, meaning that cell wall polymers are not synthesized in an oriented manner. In previous formulations of tip growth (e.g.,[35]), "transverse" or "plane" isotropy was distinguished from isotropy when considering stratification of cell wall material in the normal direction. However, in our two-dimensional formulation isotropy and transverse isotropy are the same thing, and we therefore use the word isotropy to mean isotropic in the two-dimensional sense.

Please cite this article in press as: Ohairwe et al., A fitness landscape instability governs the morphological diversity of tip-growing cells, Cell Reports (2024), https://doi.org/10.1016/j.celrep.2024.113961

Although it is unlikely that a large degree of structural anisotropy (resulting form oriented synthesis) can develop across the apical cell wall during tip growth since the polar cell wall must be isotropic, it was important to demonstrate this or demonstrate that the possibility of structural anisotropy in the cell wall does not alter our results. Here, we perform two analyses that demonstrate both of these results.

i. First, the fully anisotropic version of Equation 1 of the main text is the most general version of the linear extensibility implementation of the inflationary mechanism of cell growth:

$$\begin{pmatrix} \dot{\varepsilon}_s \\ \dot{\varepsilon}_\theta \end{pmatrix} = \underbrace{\begin{pmatrix} \gamma_s & -\gamma_{s\theta} \\ -\gamma_{s\theta} & \gamma_\theta \end{pmatrix}}_{\mathbf{\Gamma}} \begin{pmatrix} \lambda_s \\ \lambda_\theta \end{pmatrix} \quad \text{(Equation 16)}$$

The diagonal elements of $\mathbf{\Gamma}$ (γ_s and γ_θ) are the anisotropic surface extensibilities and determine how fast the wall expands in a given direction if uniaxial tension is applied in that direction. These quantities are equal at the cell pole due to rotational symmetry but may be unequal in the sub-polar cell wall if oriented cell wall polysaccharides were synthesized there. The off-diagonal element $\gamma_{s\theta}$ mechanically couples the principal directions by determining how fast the wall contracts in one direction due to uniaxial tension in the orthogonal direction. This matrix equation can be re-written:

$$\begin{aligned} \dot{\varepsilon}_s &= \gamma_s(\lambda_s - \nu\gamma_{rat}\lambda_\theta) \\ \dot{\varepsilon}_\theta &= \gamma_\theta(\lambda_\theta - \nu\lambda_s) \end{aligned} \quad \text{(Equation 17)}$$

where here $\nu = \frac{\gamma_{s\theta}}{\gamma\theta}$ and $\gamma_{rat} = \frac{\gamma_\theta}{\gamma_s}$ is the ratio between the principal surface extensibility profiles. Solving for the surface extensibility profiles, we find:

$$\begin{aligned} \gamma_\theta &= \frac{\dot{\varepsilon}_\theta}{\lambda_\theta}\frac{1}{1 - \nu\frac{\lambda_s}{\lambda_\theta}} \\ \gamma_s &= \frac{\dot{\varepsilon}_s}{\lambda_s} + \nu\gamma_\theta\frac{\lambda_\theta}{\lambda_s} \end{aligned} \quad \text{(Equation 18)}$$

where $\nu = \frac{\gamma_{s\theta}}{\gamma\theta}$ is the only quantity that we can not experimentally measure. Substituting experimental values for the principal expansion rate and tension profiles into Equation 18 reveals that for all reasonable values of $0 < \nu \lesssim 0.75$, the principal surface extensibility profiles are approximately equal across the apical cell wall (Figure S3B), indicating that the degree of anisotropy in the cell wall is negligible. Further allowing for ν to be spatially inhomogeneous allows the profiles to be precisely equal (theory not shown).

ii. Second, note that it is clear that the azimuthal surface extensibility profiles for *A. bisexualis* and *A. arbuscula* (and probably their meridional profiles) decay over two length scales, regardless of anisotropy or the flow coupling, ν (Figure S3B). That is, two length scales in the azimuthal extensibility profile is directly implied by the kinematics of tip growth of these species, independent of whether any anisotropy is present.

This result allowed us to perform a parameter space search similar to the one we performed for the isotropic case, but for the case where anisotropy develops due to the meridional surface extensibility profile decaying with one length scale. The key morphological parameters in this case are the ratio of the two length scales associated with the azimuthal surface extensibility profile and the ratio of the amplitudes of the two component profiles. We explore the case where the meridional surface extensibility profile decayed with a single length scale equal to the smaller length scale of the azimuthal profile (Figure S4A), generating anisotropy. This parameter space search gave rise to a morphospace that was very similar to the morphospace generated by the isotropic version of the model (Figure S4B). Furthermore, this morphospace possessed a cusp bifurcation that constrained natural apical morphologies in the exact same manner as that from the isotropical model (Figures S4C and S4D). In other words, the cusp catastrophe is a generic feature of inflationary tip growth that constrains the apical morphologies of tip growing cells and that does not depend on the specific molecular architecture of the cell wall. Therefore, although our data strongly suggest that the cell wall is not structurally anisotropic (Figure S3), they also implies that even if anisotropy were to develop, it does not alter any of our results.

Next, we explicitly demonstrated that structural anisotropy alone cannot explain non-rounded apical morphologies if the azimuthal surface extensibility does not decay with two distinct length scales. To do this, we simulated tip growth where the cell wall developed structural anisotropy sub-polarly by imposing that the two principal surface extensibility profiles decayed with distinct length scales, but where each one decayed over a single length scale. To simulate azimuthal structural anisotropy ($\gamma_\theta > \gamma_s$), we imposed that the azimuthal surface extensibility profile was a Gaussian that decayed over a single length scale, $l_\theta = A_\theta e^{(-s/l_\theta)^2}$ (Figure S4E). To obtain the meridional surface extensibility profile, we multiplied this first profile by a spatially dependent extensibility ratio, $\gamma_{rat} = \frac{\gamma_\theta}{\gamma_s} = (1 - \gamma_{rat})e^{(-s/l_{rat})^2} + \gamma_{rat}$ that also decayed with a single length scale, l_{rat} and where γ_{rat} is the maximum degree of anisotropy (Figure S4E). In this case, the key morphological parameters are the ratio l_{rat}/l_θ and γ_{rat}. A parameter space search across all possible morphological parameters revealed that no combination of parameters could produce highly tapered apical morphologies characteristic of *A. bisexualis* or accurately explain the curvature profile of *A. arbuscula* (Figure S4F). Indeed, nearly the entire parameter

Please cite this article in press as: Ohairwe et al., A fitness landscape instability governs the morphological diversity of tip-growing cells, Cell Reports (2024), https://doi.org/10.1016/j.celrep.2024.113961

space yielded rounded shapes with values of P1 $\lesssim 3$, whereas the majority of natural species have higher values of P1 (Figure 2F). A parallel analysis in which meridional structural anisotropy ($\gamma_s < \gamma_\theta$) developed sub-polarly revealed similar results (Figures S4G and S4H).

Finally, the anisotropical version of inflationary growth (Equation 16) provides negligible additional fitting power over the isotropical version (Equation 1; Figures 2C–2E, see above for fitting strategy).

To summarize our analysis of tip growth with structural anisotropy, analysis of the expansion rate profiles strongly suggest that the cell wall of *A. bisexualis* and *A. arbuscula* are not anisotropic (Figure S3). However, even if weak anisotropy were to develop sub-polarly, the azimuthal surface extensibility would have to decay with two length scales, which would lead to a cusp bifurcation in the morphospace that constrains natural morphologies, quantitatively similar to that observed for the isotropic case (Figure S4).

Fluorescence cell wall labeling of *A. bisexualis*

To fluorescently label the cell walls of *A. bisexualis* hyphae, we cultured them on cover-glass-bottomed slides, as above. Calcofluor white (10 μM; Sigma-Aldrich) or Direct Red23 (0.1 mg/mL, Sigma-Aldrich) were dissolved in YMM media. To control for binding kinetics of the dye, we also included 1 M sorbitol in the media, which plasmolyzes the hyphae, leaving just the cell wall. We added the dye/sorbitol media to growing hyphae and incubated fro 30 min, and then imaged. The fluorescence intensity along the cell wall was analyzed with custom MATLAB algorithms.

Transmission electron microscopy of *A. bisexualis*

A. bisexualis hyphae were fixed with 2.5% glutaraldehyde in 0.075M phosphate buffer (pH 7.2) for 30 min at room temperature, and then at overnight at 4 ° C. The samples were washed 3 times with 0.075M phosphate buffer (10 min each time), post-fixed with 1% osmium tetroxide for 1.5 h at room temperature, and dehydrated in the serial of ethanol solutions (30, 50, 70, 85, 95, 100%; 10 min each). The hyphae were then washed in acetone two times for 10 min each, infiltrated with acetone and embedded in Spurr (Electron Microscopy Sciences). Semi-thin sections (500 nm) were stained with 1% toluidine blue. Ultrathin sections (75 nm) were cut and mount on a formvar coated slot grid and stained with uranyl acetate and lead citrate by standard methods. Stained grids were imaged with Gemini300 scanning electron microscope (Zeiss) using the STEM detector at 20 kV with working distance of 3.3mm and scan speed of 8, the image pixel size is 5.6 nm.

The cell wall geometry and exocytic vesicles from TEM micrographs were extracted manually. Vesicles were binned by distance from the cell pole along the cell axis, and then mapped to the point on the cell outline at the same axial distance. The vesicles density at each point along the cell outline was then calculated as the total number of vesicles at that point divided by $2\pi rdl$, where dl is the length of a bin and r is the radius at that point.

Latrunculin B treatment of cells

Latrunculin B (abcam) was dissolved in DMSO to make a 2.5 mM master stock solution, which was further diluted 1000-fold in water to make 2.5 μM Latrunculin B stock solution. This was used to prepare yeast malt media containing 1% agarose and 80 nM latrunculin B. Molten media was poured as a thin ($\approx 3mm$) layer into petri dishes and allowed to solidify. A circular punch was used to cut out sections of this agarose. These sections were then placed on top of *A. bisexualis* hyphae that were growing in cover glass imaging chambers described above. An additional 100 μL of 80nM Latrunculin B solution was added to the top of the agar pad. The mycelia were left to grow overnight at room temperature before imaging.

To calculate the theoretical prediction of the effect of latrunculin B on cell elongation rate shown in Figure 7B, we used the expression $\rho = \pi R^2 v$, where ρ is the rate of volume increase. For the untreated case we calculated ρ by substituting experimental values of R and v, and found the predicted value of v for the latrunculin-treated cells by substituting in their mean radius, R, and the calculated value of ρ.

QUANTIFICATION AND STATISTICAL ANALYSIS

Sample sizes for each species used in the principal component analysis, that were also fit to the theoretical morphospace, are indicated in the legend of Figure 2F. Sample sizes for experimental measurements of principal expansion rates and wall tensions are indicated in the legends of Figures 3E–3G and 4A–4C. Sample size for the TEM measurements of vesicle density and cell wall fluorescence in *A. bisexualis* are indicated in Figures 3K, S6A, S6C, and S6E. Sample sizes for latrunculin B induced shape transition in *A. bisexualis* are indicated in Figures 7B and S7G. Error bars indicate ± 1 s.d. Statistical significance for treated and untreated populations was determined using Student's t-test.

Cell Reports, Volume ■ ■

Supplemental information

A fitness landscape instability governs the morphological diversity of tip-growing cells

Maxim E. Ohairwe, Branka D. Živanović, and Enrique R. Rojas

Supplementary Movie Legends

Movie S1. An *Achlya bisexualis* hypha elongating.

Movie S2. The same hypha shown in Movie S1, imaged using epifluorescence microscopy to show fluorescent microspheres adhering to the cell wall during growth.

Movie S3. An *Achlya bisexualis* hypha that was treated with 80 nM latrunculin B.

Supplementary Figure Legends

Fig. S1. Apical geometry of tip-growing cells varies across the tree of life. (A) Phase micrographs of nine tip-growing organisms. (B) Representative time-averaged meridional curvature (normalized by cell radius) versus arclength (normalized by radius) for cells from the species shown in (A). (C) Percent of morphological variation across the entire multi-species data set explained by the first five principal components. (D) Length of the cell apex versus the first principal variable. (E) Taper of the cell apex versus the first principal variable. (F) Single-value of P1 versus species. (G) Meridional curvature (normalized by cell radius) versus arclength (normalized by radius) for four values of P1 corresponding to the population-averaged values of four tip-growing species. For this calculation, the remaining principal variables were fixed to be the average experimental value across all cells from all species.

Fig. S2. Inflationary tip growth explains the mechanics of cell-wall expansion. (A) The tracks of fluorescent microspheres mapped onto the location of the cell wall during *A. bisexualis* tip growth. (B) The kinematic variables of tip growth. (C-E) Meridional speed versus arclength for *A. bisexualis*, *A. arbuscula*, and *L. longiflorum*. The profiles are representative of $n = 2, 4, 4$ cells, respectively. The orange lines are the best fit with the linear model of tip growth given by Eq. 1 of the main text. Fitting the meridional speed is equivalent to fitting the principal strain rates since the latter are calculated from the former (see (B), Eq. 5,6). Next to each profile is the sum of squared residuals (SSR) for the best fits from the isotropic (Eq. 1) and anisotropic (Eq. 16) implementations of inflationary growth, demonstrating that the anisotropic version of the model does not increase fitting power over the isotropic version. (F) The experimental principal expansion rate profiles for an *A. bisexualis* hypha, exhibiting azimuthal anisotropy. (G) A simulation of tip growth inputting the principal expansion rates shown in (F). (H) A pair of principal expansion rate profiles exhibiting isotropy found by enforcing that the two profiles both equal the mean of the experimental ones shown in (F). (I) A simulation of tip growth inputting the principal expansion rates shown in (H). (J) A pair of principal expansion rate profiles exhibiting meridional isotropy found by enforcing that the meridional expansion-rate profile equal the experimental azimuthal profile, and vice versa (i.e., by "switching" the profiles). (K) A simulation of tip growth inputting the principal expansion rates shown in (J). (L) Taper from simulations of tip growth for azimuthal anisotropy, isotropy, and meridional anisotropy, derived from experimental profiles of *A. bisexualis*, *A. arbuscula*, and *L. longiflorum* cells. (M) Schematic of structural anisotropy.

Fig. S3. The cell wall is structurally isotropic. This grid shows the principal surface extensibility profiles that are predicted from the experimental principal surface expansion rates and principal surface tensions, calculated using Eq. 18. Profiles from from one cell from each of our model systems are shown. Because if we allow for anisotropy, we cannot constrain the flow coupling, we calculate what the principal surface extensibility profiles would be, given a range of values of this parameter. This analysis demonstrates that regardless of the flow coupling, the principal surface extensibilities must be approximately anisotropic to generate the experimental surface extensibility profiles. Not shown are cases where the predicted principal surface extensibilities have regions of negative values, which is unphysical (dotted boxes).

Fig. S4. Structural anisotropy within the cell wall does not explain morphological diversity (A) Empirical anisotropic principal surface extensibility profiles. The azimuthal surface extensibility profile is a Gaussian mixture and therefore decays with two length scales, whereas the meridional profile decays with a single length scale equal to the shorter of the two length scales associated with the azimuthal profile. This creates structural anisotropy. (B) The theoretical morphospace generated by linear inflationary tip growth combined with the empirical surface extensibility profile shown in (A). P1 is the first principal component from our multispecies PCA analysis (Fig. 2F). A flow coupling of 0.5 was used. The morphospace qualitatively and quantitatively resembles the morphospace for the isotropic case (Fig. 5B). (C) Normalized radius as a function of A_{rat} for $l_{\text{rat}} = 9$. This slice through the solution manifold is indicated by the green line in Fig. (B). A_{rat} was cycled to demonstrate hysteresis. (D) Coordinates of $(l_{\text{rat}}, A_{\text{rat}})$ that, when used to simulate cell growth, yielded the best fit of the geometry for each cell of each species (white circles) overlaid onto the morphospace shown in (B). (E) Illustration of the strategy to explore the effect of azimuthal structural anisotropy on apical morphology without imposing two length scales on either of the principal surface expansion rate profiles. (left) A Gaussian azimuthal surface extensibility profile, $\gamma_\theta(s)$, that decays with a single length scale, l_θ was defined. (center) This profile was convolved with spatially dependent Gaussian anisotropy ratio, $\gamma_{\text{rat}}(s) = \gamma\theta/\gamma_{\text{s}}$, that also decayed with single length scale that was less than l_θ. (right) This produced principal surface extensibility profiles that possessed azimuthal anisotropy and each decayed with a single length scale. (F) The morphospace generated by a parameter space search across the two morphogenetic parameters associated with the principal expansion rates shown in (E) can only produce round cells (with low values of P1). (G) Illustration of the strategy to explore the effect of meridional structural anisotropy on apical morphology. (left) A Gaussian meridional surface extensibility profile, $\gamma_{\text{s}}(s)$, that decays with a single length scale, l_{s} was defined. (center) This profile was convolved with spatially dependent Gaussian anisotropy ratio, $\gamma_{\text{rat}}^{-1}(s) = \gamma_{\text{s}}/\gamma\theta$, that also decayed with single length scale that was less than l_{s}. (right) This produced principal surface extensibility profiles that possessed meridional anisotropy and each decayed with a single length scale. (H) The morphospace generated by a parameter space search across the two morphogenetic parameters associated with the principal expansion rates shown in (G) can only produce round cells (with low values of P1).

Fig. S5. The Gaussian mixture surface extensibility profile predicts apical geometry. (A-C) i) Experimental time-averaged apical geometry and meridional curvature versus arclength. ii) The apical geometry and meridional curvature generated simulations of tip growth inputting the experimentally derived surface extensibility profiles (Fig. 4A-C). iii) The apical geometry

and meridional curvature generated by simulations of tip growth inputting the experimental Gaussian mixture function (Fig. 4F) that provided the best fit of the experimentally derived surface extensibility profiles. iv) The apical geometry and meridional curvature obtained from simulations of tip growth inputting a function of the form $\gamma(s) = A_1 \cos^2(s/l_1) + A_2 \cos^2(s/l_2)$ that provided the best fit of the experimentally derived surface extensibility profiles. For C iv), the apical geometry and meridional curvature obtained from simulations of tip growth inputting a single Gaussian that provided the best fit of the experimentally derived surface extensibility profile of *L. longiflorum*.

Fig. S6. The biochemical composition of the cell wall does not change across the cell apex (A) The spatial probability distribution of vesicle density versus arclength extracted from TEM images. Confidence intervals indicate $\pm 1 s.d.$. $n = 3$ cells. (B) Representative micrograph of a cell apex stained with Direct Red 23. (C) Population-averaged fluorescence intensity versus normalized arclength of Direct Red 23-labeled cells. Confidence intervals indicate $\pm 1 s.d.$. $n = 17$ cells. (D) Representative micrograph of a cell apex stained with Calcofluor White. (E) Population-averaged fluorescence intensity versus normalized arclength of calcofluor white-labeled cells. Confidence intervals indicate $\pm 1 s.d.$. $n = 15$ cells. (F) Population-averaged normalized meridional curvature versus normalized arclength. The pink shaded area indicates the primary length scale associated with the decay of the curvature profile, and therefore also the smaller length scale associated the surface-extensibility profile.

Fig. S7. The flow coupling does not influence global morphological variation. (A) Time-averaged apical geometry for an *A. bisexualis* cell (blue line) and the apical geometry of a cell simulated using Eq. 1 of main text combined with a Gaussian mixture surface extensibility profile with l_{rat} and A_{rat} that yielded the best fit of the experimental morphology (red line). (right) The error associated with the best fit is calculated for each point used to discretize the outlines. (B) The distribution of mean error (averaged across points for a given cell) between the experimental outlines and the best fits provided the theoretical morphospaces generated by inflationary growth with a two-length-scale surface extensibility profile. The four distributions correspond to the best fits provided by morphospaces generated using 4 values of flow coupling, demonstrating that the flow coupling does not influence the fitting power of the model. (D) P1 of simulated cells using Eq. 1 of the main text and a Gaussian mixture surface extensibility profile, as a function of l_{rat} and A_{rat}, for four different values of ν. (E) Apical geometries of simulated cells for four different values of ν at a two points in the morphospace shown in (D). (F) Normalized radius as a function of A_{rat} for $l_{\text{rat}} = 9.5$. This slice through the solution manifold is indicated by the red line in Fig. 6B of the main text. The dotted section of the curve represents unstable solutions. (G) Values of $(l_{\text{rat}}, A_{\text{rat}})$ that, when used to simulate cell growth, yielded the best fit of the geometry for each cell of each species overlaid onto contours of normalized radius, and showing the empirical constraint by the bistable region of the morphospace.

Fig. S8. Chemical perturbations induce *A. bisexualis* hyphae to undergo a morphological transition. (A) The population-averaged radius of untreated *A. bisexualis* hyphae and those treated with 80 nM latrunculin B. Error bars indicate ± 1 s.d. $n = 11$ and 9 hyphae for untreated and treated cells, respectively. (B) Diagram explaining why global softening of a two-length-

scale surface extensibility profile increases A_{rat}. (C) Brightfield micrograph of a *A. bisexualis* hypha growing in 350 mM sorbitol. (D) The population-averaged radius of untreated *A. bisexualis* hyphae and those treated with 350 mM sorbitol. Error bars indicate ± 1 s.d. $n = 11$ and 9 hyphae for untreated and treated cells, respectively. (E) The population-averaged elongation rate of untreated *A. bisexualis* hyphae and those treated with 350 mM sorbitol. Error bars indicate ± 1 s.d. $n = 9$ and 12 hyphae for untreated and treated cells, respectively.

Supplementary Figures

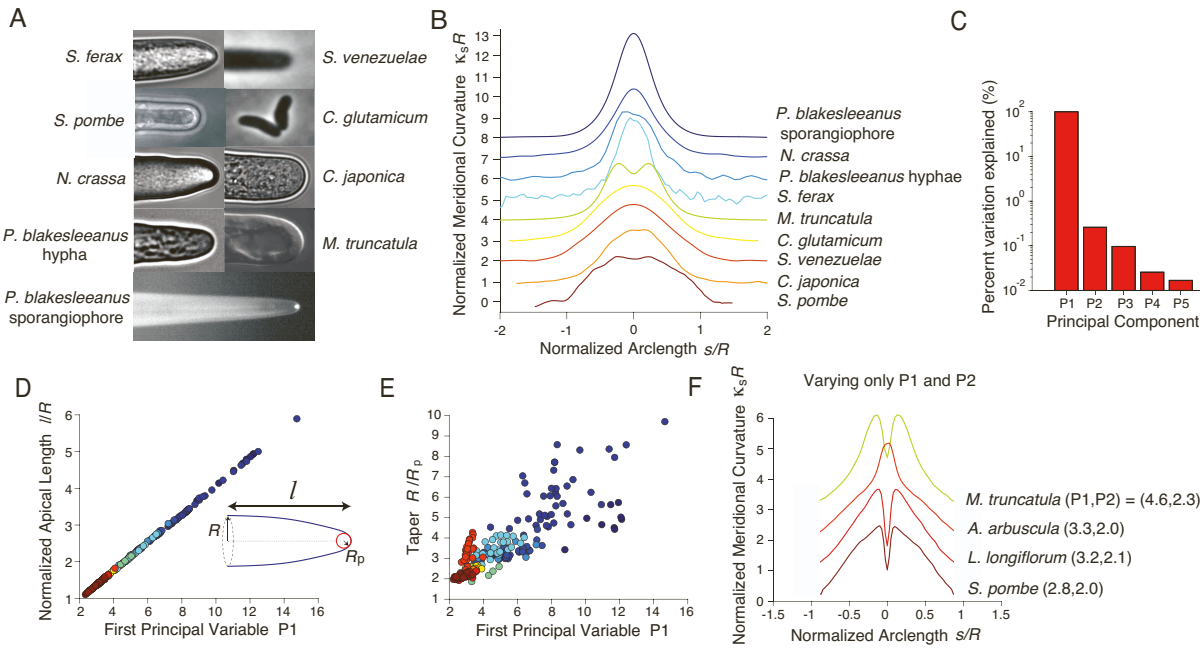

Figure S1

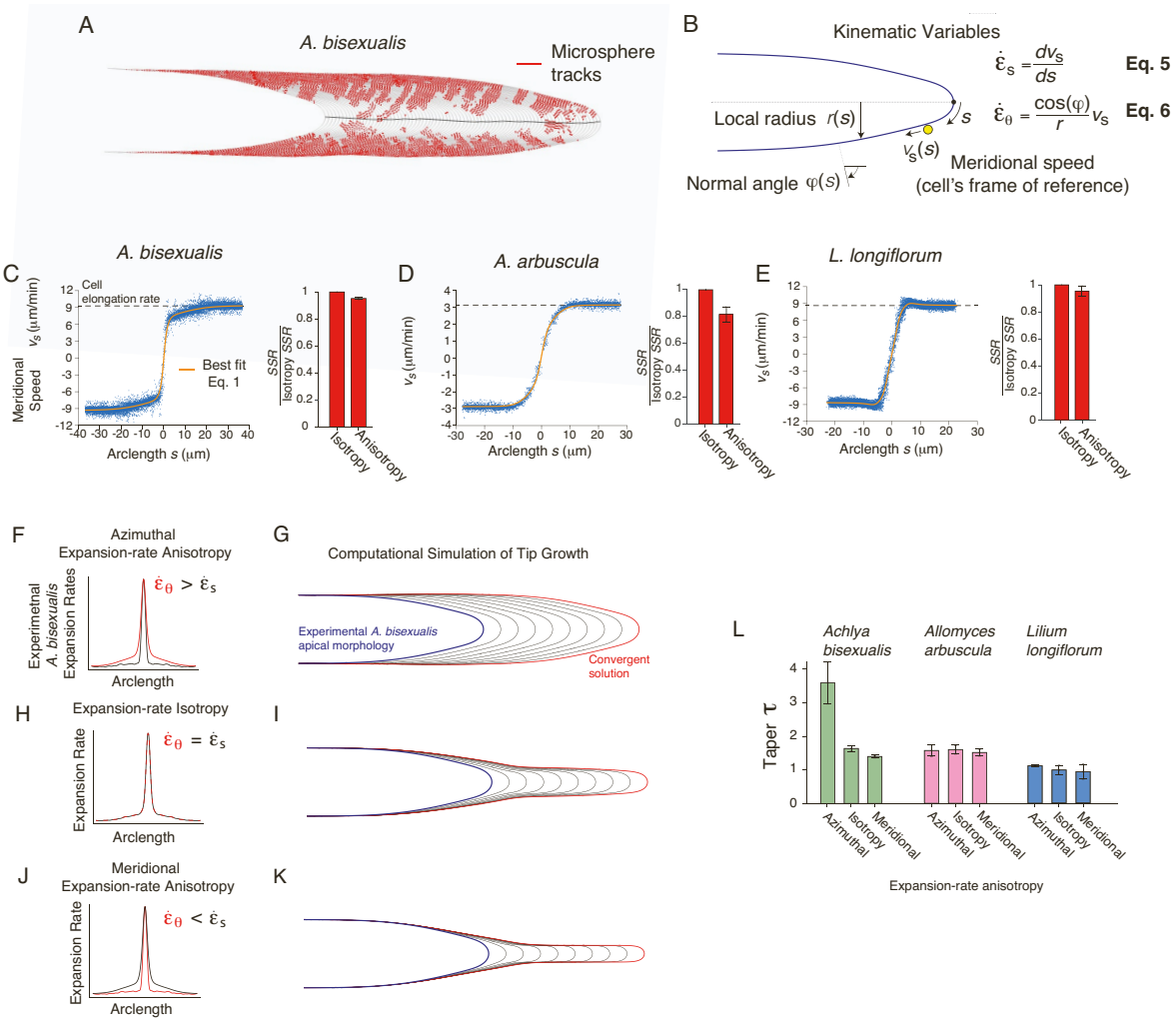
A
A. bisexualis
Microsphere tracks
B
Kinematic Variables
Eq. 5
Eq. 6
Local radius r(s)
Normal angle φ(s)
Meridional speed
(cell's frame of reference)
C
A. bisexualis
Cell elongation rate
Best fit Eq. 1
Meridional Speed
Arclength s (μm)
SSR
Isotropy
Anisotropy
D
A. arbuscula
E
L. longiflorum
F
Azimuthal Expansion-rate Anisotropy
Experimetnal A. bisexualis Expansion Rates
Arclength
G
Computational Simulation of Tip Growth
Experimental A. bisexualis apical morphology
Convergent solution
H
Expansion-rate Isotropy
Expansion Rate
I
J
Meridional Expansion-rate Anisotropy
K
L
Achlya bisexualis
Allomyces arbuscula
Lilium longiflorum
Taper τ
Azimuthal
Isotropy
Meridional
Expansion-rate anisotropy

Figure S2

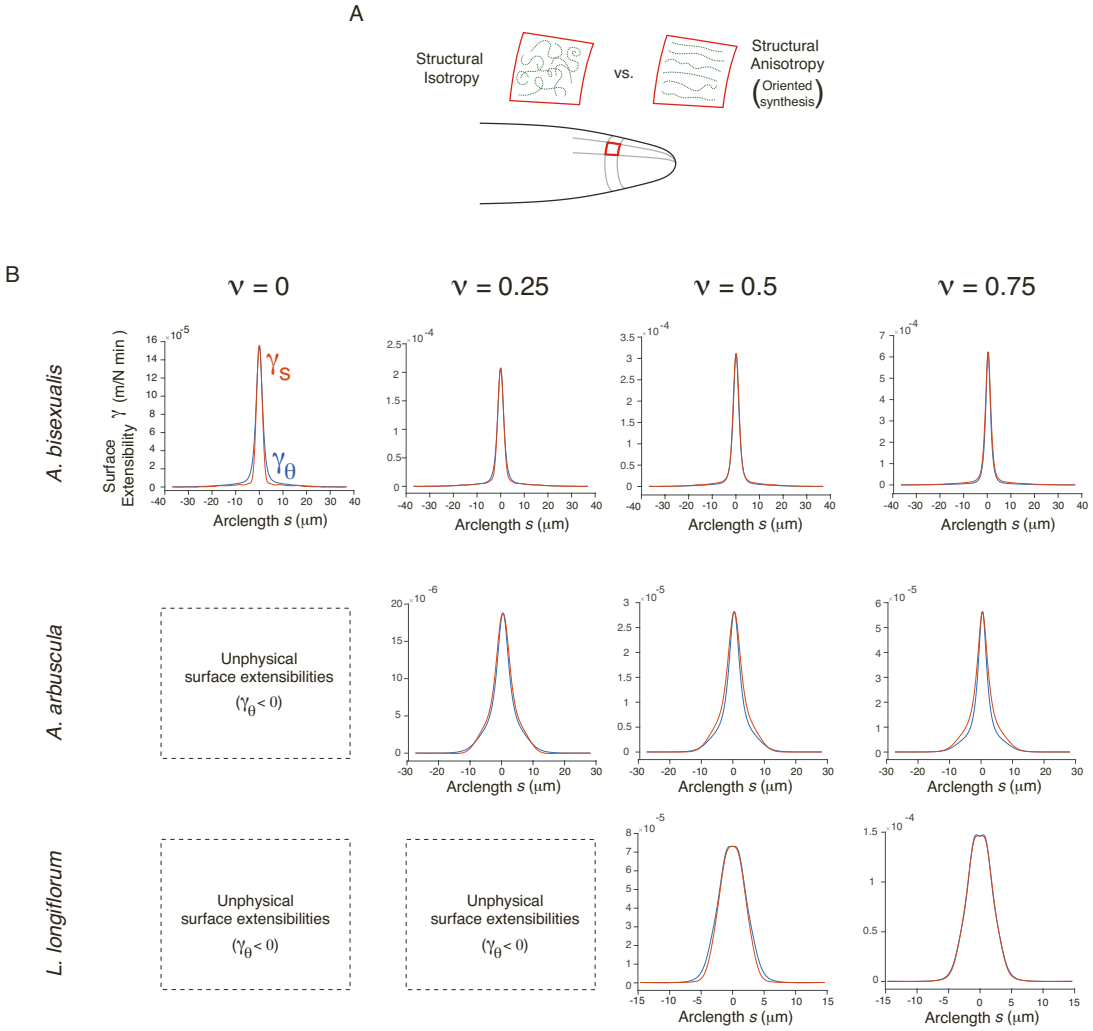
A
Structural Isotropy
vs.
Structural Anisotropy
(Oriented synthesis)
B
ν = 0
ν = 0.25
ν = 0.5
ν = 0.75
A. bisexualis
A. arbuscula
L. longiflorum
Surface Extensibility γ (m/N min)
γs
γθ
Arclength s (μm)
Unphysical surface extensibilities
(γθ < 0)

Figure S3

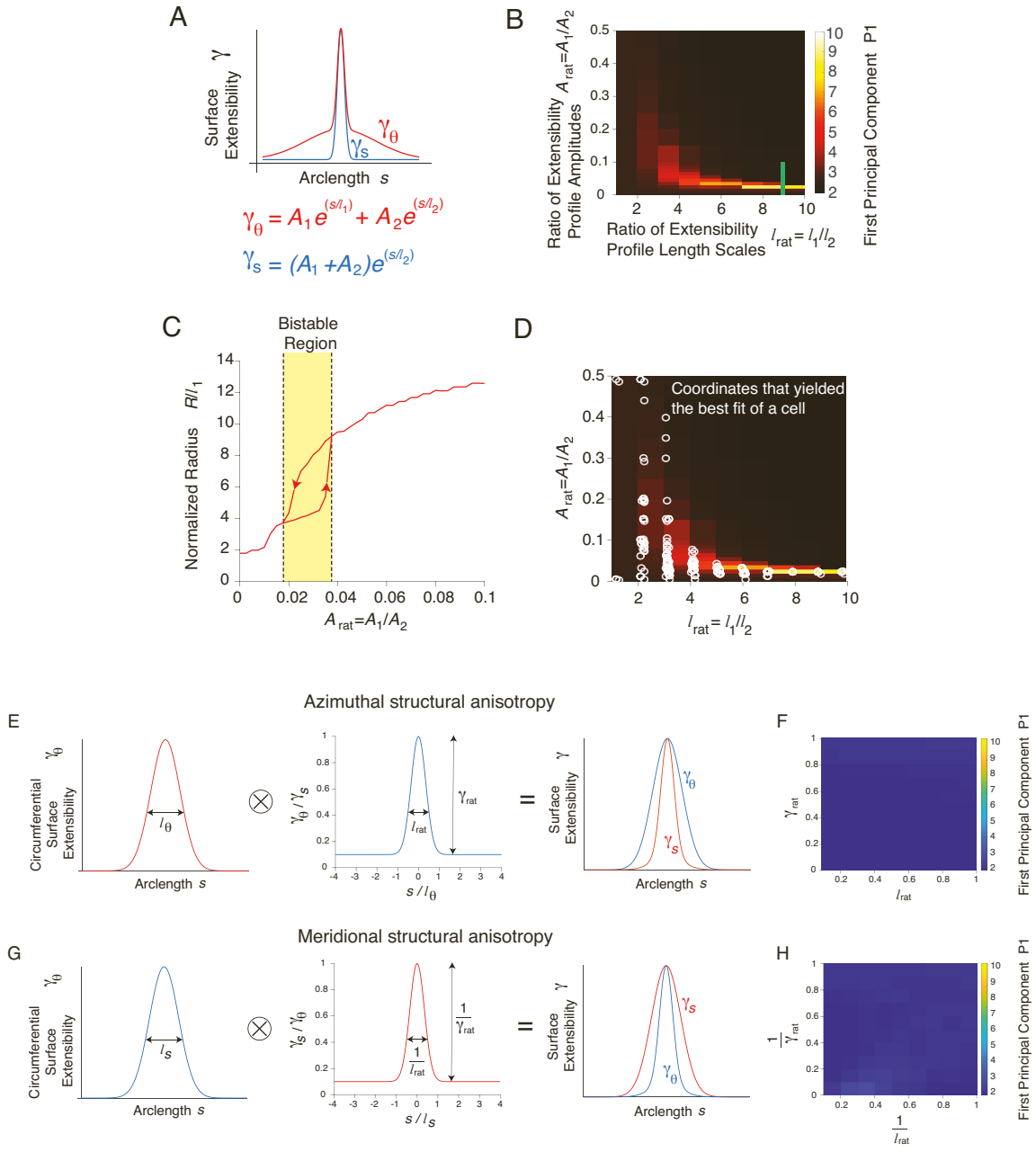
A
Surface Extensibility γ
γθ
γs
Arclength s
γθ = A1e^(s/l1) + A2e^(s/l2)
γs = (A1 +A2)e^(s/l2)
B
Ratio of Extensibility Profile Amplitudes Arat=A1/A2
Ratio of Extensibility Profile Length Scales lrat= l1/l2
First Principal Component P1
C
Bistable Region
Normalized Radius R/l1
Arat=A1/A2
D
Coordinates that yielded the best fit of a cell
Arat=A1/A2
lrat= l1/l2
Azimuthal structural anisotropy
E
Circumferential Surface Extensibility γθ
lθ
Arclength s
γθ / γs
γrat
lrat
s / lθ
Surface Extensibility γ
γθ
γs
Arclength s
F
γrat
lrat
First Principal Component P1
Meridional structural anisotropy
G
Circumferential Surface Extensibility γθ
ls
Arclength s
γs / γθ
1/γrat
1/lrat
s / ls
Surface Extensibility γ
γs
γθ
Arclength s
H
1/γrat
1/lrat
First Principal Component P1

Figure S4

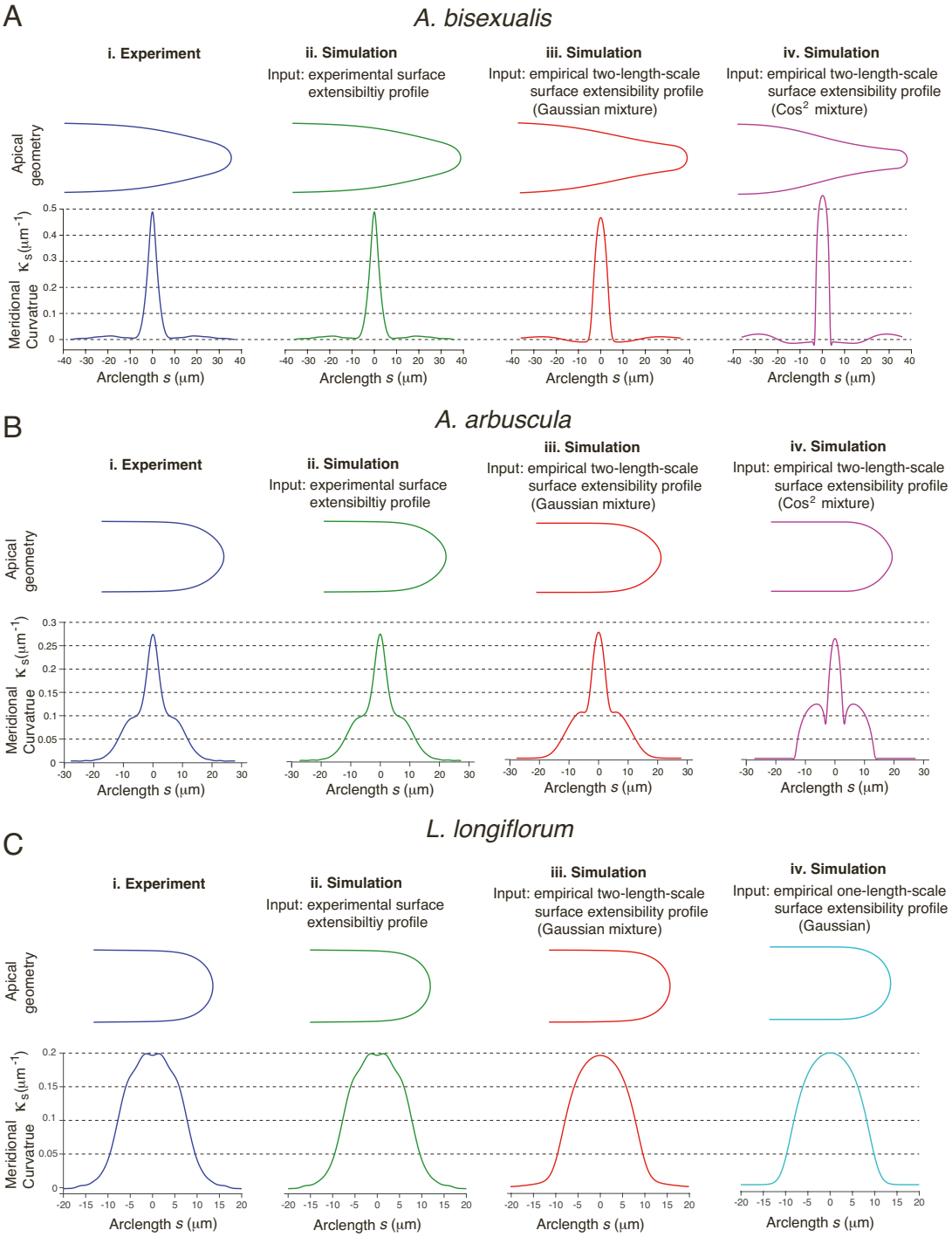
A
A. bisexualis
i. Experiment
ii. Simulation
Input: experimental surface extensibiltiy profile
iii. Simulation
Input: empirical two-length-scale surface extensibility profile (Gaussian mixture)
iv. Simulation
Input: empirical two-length-scale surface extensibility profile (Cos² mixture)
Apical geometry
Meridional Curvatrue κs(μm-1)
Arclength s (μm)
B
A. arbuscula
i. Experiment
ii. Simulation
Input: experimental surface extensibiltiy profile
iii. Simulation
Input: empirical two-length-scale surface extensibility profile (Gaussian mixture)
iv. Simulation
Input: empirical two-length-scale surface extensibility profile (Cos² mixture)
Apical geometry
Meridional Curvatrue κs(μm-1)
Arclength s (μm)
C
L. longiflorum
i. Experiment
ii. Simulation
Input: experimental surface extensibiltiy profile
iii. Simulation
Input: empirical two-length-scale surface extensibility profile (Gaussian mixture)
iv. Simulation
Input: empirical one-length-scale surface extensibility profile (Gaussian)
Apical geometry
Meridional Curvatrue κs(μm-1)
Arclength s (μm)

Figure S5

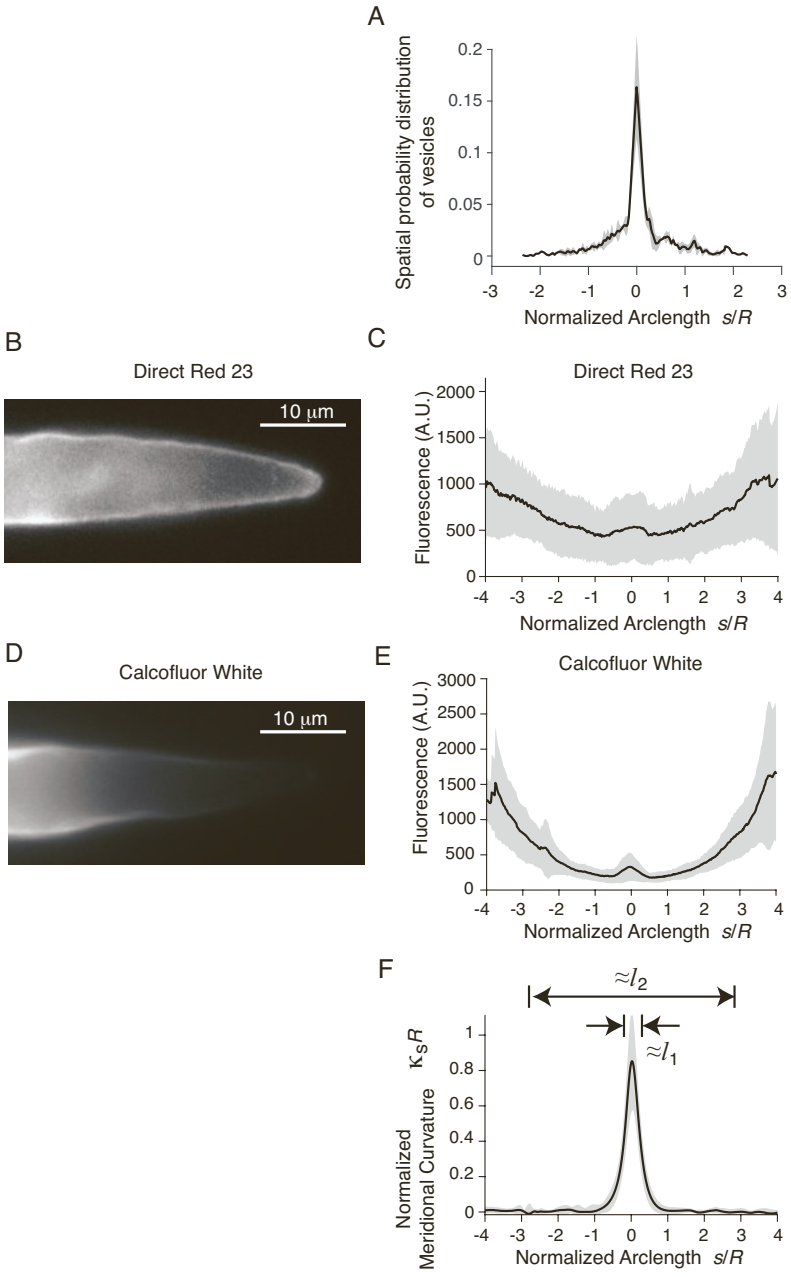
A
Spatial probability distribution of vesicles
0.2
0.15
0.1
0.05
0
-3 -2 -1 0 1 2 3
Normalized Arclength s/R
B
Direct Red 23
10 μm
C
Direct Red 23
Fluorescence (A.U.)
2000
1500
1000
500
0
-4 -3 -2 -1 0 1 2 3 4
Normalized Arclength s/R
D
Calcofluor White
10 μm
E
Calcofluor White
Fluorescence (A.U.)
3000
2500
2000
1500
1000
500
0
-4 -3 -2 -1 0 1 2 3 4
Normalized Arclength s/R
F
≈l2
≈l1
κsR
Normalized Meridional Curvature
1
0.8
0.6
0.4
0.2
0
-4 -3 -2 -1 0 1 2 3 4
Normalized Arclength s/R

Figure S6

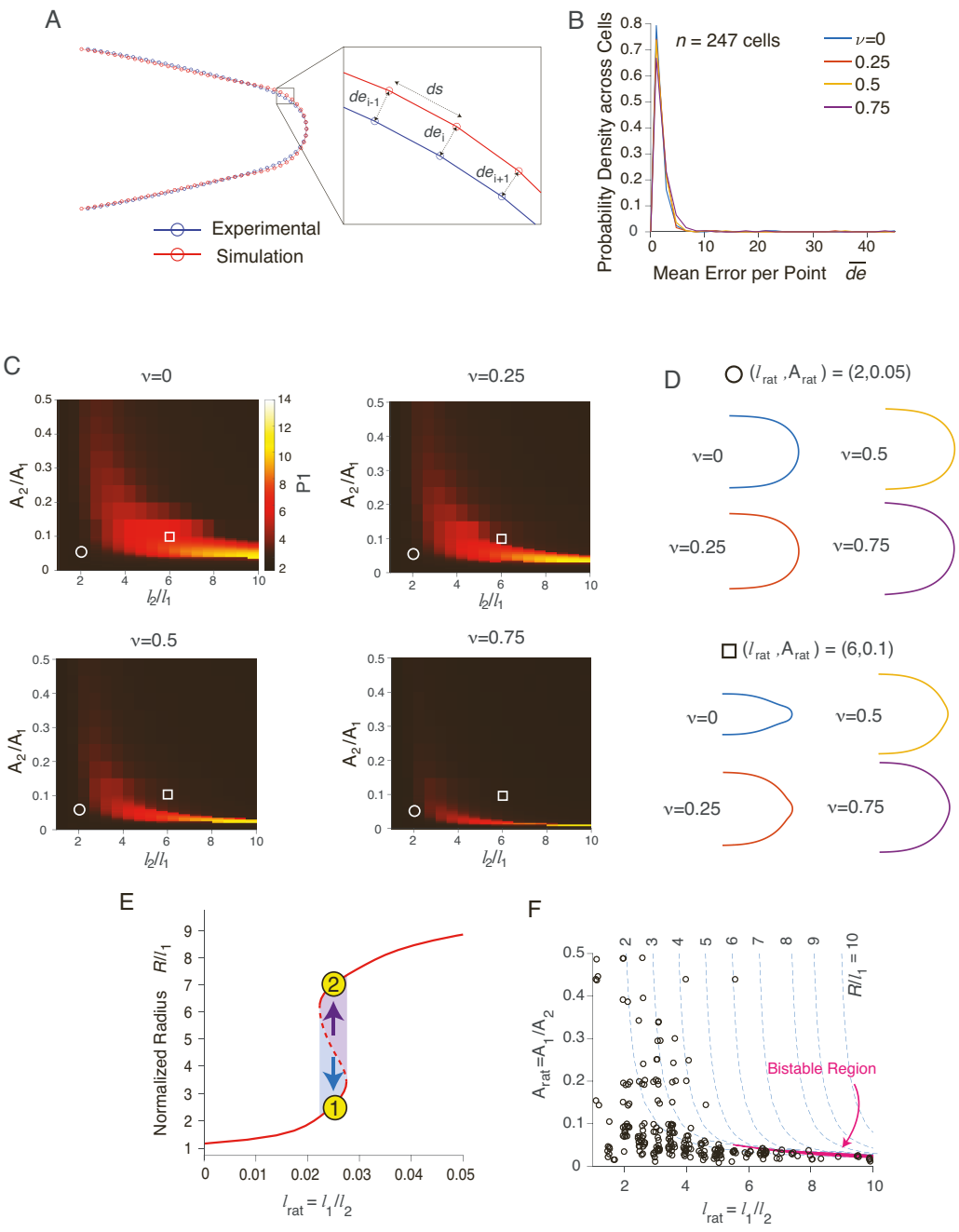
A
Experimental
Simulation
B
n = 247 cells
ν=0
0.25
0.5
0.75
Probability Density across Cells
Mean Error per Point
C
ν=0
ν=0.25
ν=0.5
ν=0.75
P1
D
(l_rat ,A_rat) = (2,0.05)
(l_rat ,A_rat) = (6,0.1)
E
Normalized Radius
F
Bistable Region

Figure S7

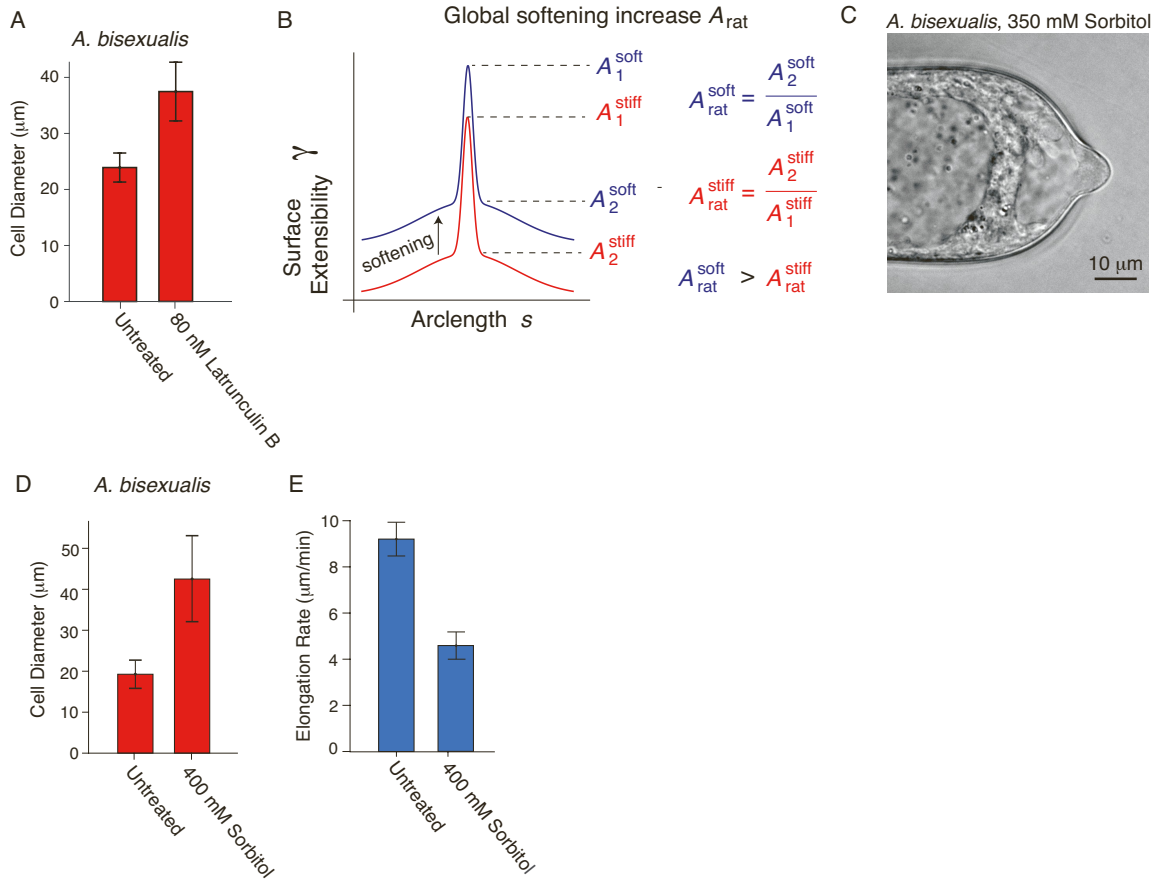
A
A. bisexualis
Cell Diameter (μm)
0
10
20
30
40
Untreated
80 nM Latrunculin B
B
Global softening increase A_{rat}
Surface Extensibility γ
softening
Arclength s
A_1^{soft}
A_1^{stiff}
A_2^{soft}
A_2^{stiff}
$A_{rat}^{soft} = \frac{A_2^{soft}}{A_1^{soft}}$
$A_{rat}^{stiff} = \frac{A_2^{stiff}}{A_1^{stiff}}$
$A_{rat}^{soft} > A_{rat}^{stiff}$
C
A. bisexualis, 350 mM Sorbitol
10 μm
D
A. bisexualis
Cell Diameter (μm)
0
10
20
30
40
50
Untreated
400 mM Sorbitol
E
Elongation Rate (μm/min)
0
2
4
6
8
10
Untreated
400 mM Sorbitol

Figure S8